We are IntechOpen,
the world's leading publisher of
Open Access books
Built by scientists, for scientists

6,900
Open access books available

186,000
International authors and editors

200M
Downloads

Our authors are among the

154
Countries delivered to

TOP 1%
most cited scientists

12.2%
Contributors from top 500 universities

CLARIVATE ANALYTICS
BOOK CITATION INDEX
INDEXED

WEB OF SCIENCE™

Selection of our books indexed in the Book Citation Index
in Web of Science™ Core Collection (BKCI)

Interested in publishing with us?
Contact book.department@intechopen.com

Numbers displayed above are based on latest data collected.
For more information visit www.intechopen.com

Atomic and Molecular Low-n Rydberg States in Near Critical Point Fluids[*]

Luxi Li, Xianbo Shi, Cherice M. Evans and Gary L. Findley

Additional information is available at the end of the chapter

1. Introduction

Since electronic excited states are sensitive to the local fluid environment, dopant electronic transitions are an appropriate probe to study the structure of near critical point fluids (i.e., perturbers). In comparison to valence states, Rydberg states are more sensitive to their environment [1]. However, high-n Rydberg states are usually too sensitive to perturber density fluctuations, which makes these individual dopant states impossible to investigate. (Nevertheless, under the assumption that high-n Rydberg state energies behave similarly to the ionization threshold of the dopant, dopant high-n Rydberg state behavior in supercritical fluids can be probed indirectly by studying the energy of the quasi-free electron, through photoinjection [2–11] and field ionization [12–19].) Low-n Rydberg states, on the other hand, are excellent spectroscopic probes to investigate excited state/fluid interactions.

The study of low-n Rydberg states in dense fluids began with the photoabsorption of alkali metals in rare gas fluids [20, 21]. Later researchers expanded the investigation into rare gas dopants in supercritical rare gas fluids [22–26], and molecular dopants in atomic and molecular perturbers [27–36]. However, none of these previous groups studied dilute solutions near the critical point of the solvent. (The single theoretical study of a low-n Rydberg state in a near critical point fluid was performed by Larrégaray, *et al.* [35]; this investigation predicted a change in the line shape and in the perturber induced shift of the Rydberg transition.) These results from previous experimental and theoretical investigations of low-n Rydberg states in dense fluids are reviewed in Section 2.

In this Chapter, we present a systematic investigation of the photoabsorption of atomic and molecular dopant low-n Rydberg transitions in near critical point atomic fluids [37–40]. The individual systems probed allowed us to study (dopant/perturber) atomic/atomic interactions (i.e., Xe/Ar) and molecular/atomic interactions (i.e., CH_3I/Ar, CH_3I/Kr, CH_3I/Xe) near the perturber critical point. The experimental techniques and theoretical

---

[*]This work is adapted from that originally submitted by Luxi Li to the faculty of the Graduate Center of the City University of New York in partial fulfillment of the requirements for the degree of Doctor of Philosophy.

methodology for this extended study of dopant/perturber interactions are discussed in Section 3. Section 4 presents a review of our results for low-n atomic and molecular Rydberg states in atomic supercritical fluids. The accuracy of a semi-classical statistical line shape analysis is demonstrated, and the results are then used to obtain the perturber-induced energy shifts of the primary low-n Rydberg transitions. A striking critical point effect in this energy shift was observed for all of the dopant/perturber systems presented here. A discussion of the ways in which the dopant/perturber interactions influence the perturber-induced energy shift is also presented in Section 4. We conclude with an explanation of the importance of the inclusion of three-body interactions in the line-shape analysis, and with a discussion of how this model changes when confronted with non-spherical perturbers and polar fluids.

2. Perturber effects on low-n Rydberg states

2.1. Supercritical fluids

A supercritical fluid (SCF) exists at a temperature higher than the critical temperature and, therefore, has properties of both a liquid and a gas [41]. For example, SCFs have the large compressibility characteristic of gases, but the potential to solvate materials like a liquid. Moreover, near the critical point the correlation length of perturber molecules becomes unbounded, which induces an increase in local fluid inhomogeneities [41].

The local density $\rho(r)$ of a perturbing fluid around a central species (either the dopant or a single perturber) is defined by [42, 43]

$$\rho(r) \; = \; g(r)\,\rho\,,$$

where $g(r)$ is the radial distribution function and ρ is the bulk density. For neat fluids and for most dilute dopant/perturber systems, the interactions between the species in the system are attractive in nature. Thus, the perturber forms at least one solvent shell around the dopant (or a central perturber). As the dilute dopant/perturber system approaches the critical density and temperature of the perturber, the intermolecular interactions increase. This increase leads to a change in the behavior of the local density as a function of the bulk density [41]. Therefore, the changes in fluid properties near the critical point are due to the higher correlation between the species in the fluid. These intermolecular correlations are usually probed spectroscopically by dissolving a dopant molecule in the SCF. Since electronic excited states are incredibly sensitive to local fluid environment, fluctuations in the fluid environment can be investigated by monitoring variations in the absorption or emission of the dopant.

Fig. 1 gives three example spectroscopic studies of a dopant in near critical point SCFs. Fig 1a shows the energy position of an anthracene emission line for anthracene doped into near critical point carbon dioxide [44]. Unfortunately, no emission data on non-critical isotherms were measured in this fluorescence emission study. However, the maximum emission position shows a striking critical effect in comparison to a calculated baseline. A more complete investigation of temperature effects on the local density of SCFs via UV photoabsorption [45] of ethyl p-(N,N-dimethylamino)benzoate (DMAEB) in supercritical CHF_3 is presented in Fig. 1b for three isotherms near the critical isotherm. The isotherms shown are at the reduced temperature T_r [where $T_r \equiv T/T_c$ with T_c being the critical temperature of the fluid] of 1.01, 1.06 and 1.11. Although the three isotherms are evenly spaced, the photoabsorption shifts are very similar on the $T_r = 1.06$ and $T_r = 1.11$ isotherms, while the shift on the

$T_r = 1.01$ isotherm is significantly different. Therefore, the perturber induced shift is only temperature sensitive near the critical point of the perturber. Urdahl, *et al.* [46, 47] studied the $W(CO)_6$ T_{1u} asymmetric CO stretching mode doped into supercritical carbon dioxide, ethane and trifluoromethane by IR photoabsorption. All three systems show similar behavior, an example of which is presented in Fig. 1c. Again, the absorption band position changes significantly along the critical isotherm near the critical density. However, extracting the data presented in Fig. 1 is difficult. Moreover, most of the previous work [41] has used dopant valence transitions as probes, and these states tend to be less sensitive to local environments [1]. In the present work, we investigate near critical point SCFs using low-*n* Rydberg state transitions as the probe. Since Rydberg states are hydrogen-like, it should be possible to model these states within the statistical mechanical theory of spectral line-broadening.
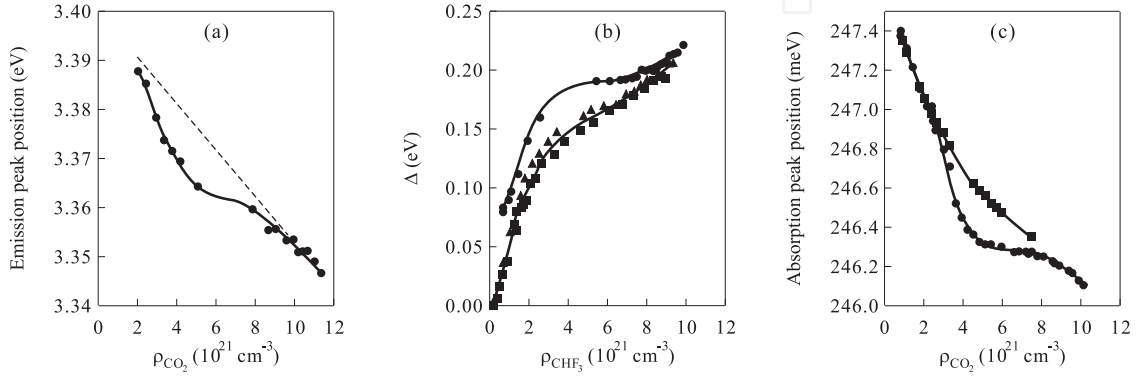

Figure 1. (a) The energy of fluorescence emission for (•) anthracene doped into supercritical carbon dioxide at a reduced temperature $T_r \simeq 1.01$ plotted as a function of carbon dioxide number density ρ_{CO_2}. The dashed line (- - -) is a reference line calculated using perturber bulk densities. Adapted from [44]. (b) The perturber induced energy shifts of the photoabsorption maximum for DMAEB doped into supercritical CHF_3 at (•) 30.0°C [i.e., $T_r \simeq 1.01$], (▲) 44.7°C, and (■) 59.6°C, plotted as a function of CHF_3 number density ρ_{CHF_3}. Adapted from [45]. (c) The energy position of infrared absorption for the $W(CO)_6$ CO stretching mode in supercritical carbon dioxide at (•) 33°C [i.e., $T_r \simeq 1.01$] and at (■) 50°C, plotted as a function of ρ_{CO_2}. Adapted from [46, 47]. The solid lines in (a) - (c) are provided as a visual aid.

2.2. Theoretical model

Due to the hydrogenic properties of Rydberg states, the optical electron is in general insensitive to the structure of the cationic core. Therefore, both atomic and molecular Rydberg transitions can be modeled within the same theory. In a very dilute dopant/perturber system, assuming that the dopant Rydberg transition is at high energy [i.e. $\beta (E_g - E_e) \gg 1$, $\beta = 1 / (k T)$], the Schrödinger equation is

$$H|\Psi\rangle = E|\Psi\rangle , \tag{1}$$

where the eigenfunction $|\Psi\rangle$ is a product of the dopant electronic wavefunction $|\alpha\rangle$ and the individual perturber wavefunctions $|\psi_i; \alpha\rangle$. The Hamiltonian H in eq. (1) is the sum of several individual Hamiltonians, namely the Hamiltonian for the free dopant, the Hamiltonian for the free perturber, and the Hamiltonian for the dopant/perturber intermolecular correlation. The Hamiltonian H_{FD} for the free dopant is [48]

$$H_{FD} = \sum_\alpha E_\alpha |\alpha\rangle \langle\alpha| , \tag{2}$$

where $\alpha = e, g$ with e and g representing the excited state and ground state of the free dopant. The Hamiltonian H_{FP} for the free non-interacting perturber is given by [48]

$$H_{FP} = -\sum_i^N \frac{\hbar^2}{2\,m} \nabla_i^2 \,, \tag{3}$$

where N is the total number of perturbing atoms in the range of the Rydberg optical electron. Finally, the Hamiltonian H_{PD} for the intermolecular interaction is [48]

$$H_{PD} = \sum_\alpha \sum_i [V_\alpha(r_i) + V'(r_i)] |\Psi\rangle\langle\Psi| \,, \tag{4}$$

where $V(r)$ is the dopant/perturber intermolecular potential, and $V'(r)$ is the perturber/perturber intermolecular potential. Therefore, the total Hamiltonian H is [48]

$$H = H_{FD} + H_{FP} + H_{PD} \,, \tag{5}$$

which can be rewritten as a ground state Hamiltonian expectation value H_g and an excited state Hamiltonian expectation value H_e.

The absorption coefficient function is given as the Fourier transform [48]

$$\mathfrak{L}(\omega) \equiv \frac{1}{2\,\pi} \int_{-\infty}^{\infty} dt \, \mathrm{e}^{-i\,\omega\,t} \langle \vec{\mu}(0) \cdot \vec{\mu}(t) \rangle \,, \tag{6}$$

where the autocorrelation function (i.e., $\langle \cdots \rangle$) is the thermal average of the scalar product of the dipole moment operator (i.e., $\vec{\mu}$) of the dopant at two different times. This autocorrelation function can be resolved within the Liouville operator formalism to give [48]

$$\langle \vec{\mu}(0) \cdot \vec{\mu}(t) \rangle \equiv \exp\left[\rho_P \langle \mathrm{e}^{i\,L_g\,t} - 1 \rangle_g\right] \,, \tag{7}$$

where the two-body Liouville operator L_g is defined by

$$L_g \Omega = H_e \Omega - \Omega H_g = [H_g, \Omega] + (E_e - E_g)\Omega \,, \tag{8}$$

where Ω is an arbitrary operator. However, if lifetime broadening is neglected, only the dopant/perturber interaction and the dopant electronic energy change during the transition. Therefore, the autocorrelation function can be rewritten as [48]

$$\langle \vec{\mu}(0) \cdot \vec{\mu}(t) \rangle \equiv \mathrm{e}^{i\,\omega_0\,t} \exp\left[\rho_P \langle \mathrm{e}^{i\,\Delta V\,t} - 1 \rangle_g\right] \,, \tag{9}$$

where ω_0 is the transition frequency of the neat dopant, ρ_P is the perturber density, and $\Delta V = V_e - V_g$, with V_e and V_g being the excited-state dopant/ground-state perturber and ground-state dopant/ground-state perturber intermolecular potentials, respectively.

In semi-classical line shape theory, the line shape function for an allowed transition is given by [20],

$$\mathfrak{L}(\omega) = \frac{1}{2\,\pi} \int_{-\infty}^{\infty} dt \, \mathrm{e}^{-i\,[\omega(\mathbf{R}) - \omega_0]\,t} \, \frac{Z\,(\beta\,V_g + i\,t\,\Delta V)}{Z\,(\beta\,V_g)} \,, \tag{10}$$

where Z is the partition function and $\mathbf{R}$ denotes the collection of all dopant/perturber distances. Under the classical fluid approximation of Percus [49–51], the autocorrelation function $\Phi(t)$ is given by a density expansion [20]

$$\Phi(t) = \ln Z(\beta V_g + i t \Delta V) - \ln Z(\beta V_g) = A_1(t) + A_2(t) + \cdots, \tag{11}$$

where [20, 25]

$$A_n(t) = \frac{1}{n!} \int \cdots \int \prod_{j=1}^n d^3 R_j \, \mathfrak{F}(\mathbf{R}_1, \ldots, \mathbf{R}_n)$$
$$\times \prod_{j=1}^n \left[\exp(-i \, \Delta V(\mathbf{R}_j) \, t) - 1 \right]. \tag{12}$$

In eq. (12), $\mathfrak{F}(\mathbf{R}_1, \ldots, \mathbf{R}_n)$ is the Ursell distribution function [25, 26, 49–51], and $\Delta V(\mathbf{R}) = V_e(\mathbf{R}) - V_g(\mathbf{R})$. The Ursell distribution function for two body interactions [25, 26] is $\mathfrak{F}(\mathbf{R}) = \rho_P \, g_{PD}(\mathbf{R})$, where $g_{PD}(\mathbf{R})$ is the perturber/dopant radial distribution function. The three body Ursell distribution function is estimated using the Kirkwood superposition approximation [52] to be

$$\mathfrak{F}(\mathbf{R}_1, \mathbf{R}_2) = \rho_P^2 \left[g_{PP}(|\mathbf{R}_1 - \mathbf{R}_2|) - 1 \right] g_{PD}(\mathbf{R}_1) \, g_{PD}(\mathbf{R}_2), \tag{13}$$

where $g_{PP}(\mathbf{R})$ is the perturber/perturber radial distribution function. The density expansion terms are multibody interactions between dopant and perturber over all space. $A_1(t)$ is the dopant/perturber two-body interaction, $A_2(t)$ is the dopant/perturber three-body interaction, and $A_n(t)$ is the dopant/perturber $n + 1$ body interaction. Substitution of these Ursell distribution functions into eq. (12) under the assumption of spherically symmetric potentials, gives [25, 26, 37]

$$A_1(t) = 4 \pi \rho_P \int_0^\infty dr \, r^2 \, g_{PD}(r) \left[e^{-i t \Delta V(r)} - 1 \right], \tag{14}$$

and

$$A_2(t) = 4 \pi \rho_P^2 \int_0^\infty dr_1 \, r_1^2 \, g_{PD}(r_1) \left[e^{-i t \Delta V(r_1)} - 1 \right]$$
$$\times \int_0^\infty dr_2 \, r_2^2 \, g_{PD}(r_2) \left[e^{-i t \Delta V(r_2)} - 1 \right]$$
$$\times \frac{1}{r_1 r_2} \int_{|r_1 - r_2|}^{|r_1 + r_2|} s \left[g_{PP}(s) - 1 \right] ds. \tag{15}$$

Since the strength of the interaction decreases as the number of bodies involved increases, and since higher order interactions are more difficult to model, most line shape simulations are truncated at the second term $A_2(t)$.

The autocorrelation function can be written as a power series expansion at $t = 0$, namely [21, 48, 53, 54]

$$\Phi(t) = \sum_{n=1}^\infty \frac{i^n}{n!} \, m_n \, t^n, \tag{16}$$

where the expansion coefficients m_i are given by

$$m_n = \frac{1}{(\sqrt{-1})^n} \frac{d^n}{dt^n} \Phi(t) \Big|_{t=0}. \tag{17}$$

Using eq. (11) with $A_1(t)$ and $A_2(t)$ from eqs. (14) and (15), the first two expansion coefficients become [25]

$$m_1 = -4\pi\rho_{\text{P}}\int_0^\infty dr\, r^2\, g_{\text{PD}}(r)\,\Delta V(r)\,, \tag{18}$$

and

$$m_2 = m_1^2 + 4\pi\rho_{\text{P}}\int_0^\infty dr\, r^2\, g_{\text{PD}}(r)\,\Delta V(r)^2$$

$$+ 8\pi^2\rho_{\text{P}}^2\int_0^\infty\int_0^\infty dr_1\, dr_2\, r_1\, r_2\, g_{\text{PD}}(r_1)\, g_{\text{PD}}(r_2) \tag{19}$$

$$\times\,\Delta V(r_1)\,\Delta V(r_2)\int_{|r_1-r_2|}^{|r_1+r_2|} s\,[\,g_{\text{PP}}(s)-1\,]\,ds\,.$$

The above expansion coefficients are equivalent to the moments of the optical coefficient, which are defined as [25]

$$m_n = \int \mathcal{L}(E)\,E^n\,dE\,. \tag{20}$$

Thus, the perturber induced shift $\Delta(\rho_{\text{P}})$ in the energy position of the optical coefficient maximum is [25, 26]

$$\Delta(\rho_{\text{P}}) = M_1 = \frac{m_1}{m_0} = \int \mathcal{L}(E)\,E\,dE \Big/ \int \mathcal{L}(E)\,dE\,, \tag{21}$$

while the full-width-half-maximum of the experimental absorption spectrum is proportional to

$$M_2 = \left[\frac{m_2}{m_0}-M_1^2\right]^{1/2} = \left[\left(\int \mathcal{L}(E)\,E^2\,dE \Big/ \int \mathcal{L}(E)\,dE\right)-M_1^2\right]^{1/2}\,, \tag{22}$$

where $\mathcal{L}(E)$ is the absorption band for the transition and $E = \hbar(\omega-\omega_0)$ [$\hbar \equiv$ reduced Planck constant].

2.3. Previous studies

The interaction of dopant low-n Rydberg states with dense fluids has previously been the subject of some interest both experimentally and theoretically [1, 22–36]. The first detailed investigation of these interactions was a study of Xe low-n Rydberg states doped into the dense rare gas fluids (i.e., argon, neon and helium) by Messing, et al. [25, 26]. In the same year, Messing, et al. [27, 28] presented their studies of molecular low-n Rydberg states in dense Ar and Kr. A decade later, Morikawa, et al. [34] probed the NO valence and low-n Rydberg state transitions in dense argon and krypton. All of these experiments [25–28, 34] used a basic moment analysis of absorption bands to determine the energy shifts of these bands as a function of perturber number density. The photoabsorption energy shifts were then simulated [25–28, 34] using eq. (18) for various assumptions of intermolecular potentials and radial distribution functions. Messing, et al. also performed line shape simulations under the assumption of a Gaussian line shape [25–28] for selected perturber number densities. As molecular dynamics developed, research groups [30, 31, 33, 35, 36] returned to absorption line shape simulations in an attempt to match the asymmetric broadening observed experimentally.
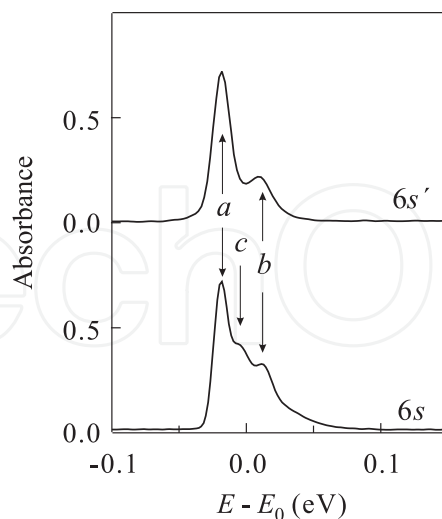
2.3.1. Xe in Ar, Ne and He

Figure 2. Photoabsorption spectra (relative units) of the Xe 6*s* and 6*s*′ transitions doped into Ar at an argon number density of $\rho_{Ar} = 1.47 \times 10^{21}$ cm^{-3} and a temperature of 23.6°C. *a* corresponds to eq. (23), *b* to eq. (24), and *c* to eq. (25). For the 6*s* Rydberg state $E_0 = 8.437$ eV and for the 6*s*′ Rydberg state $E_0 = 9.570$ eV. Data from the present work.

When Xe 6*s* and 6*s*′ Rydberg state transitions are excited in the presence of low density argon or krypton, satellite bands appear on the higher energy wing of the absorption or emission spectra [22–24]. These blue satellite bands increase with increasing perturber density [22–24] and with decreasing temperature. Therefore, Castex, *et al.* [22–24] concluded that these blue satellites are caused by the formation of dopant/perturber ground state and excited state dimers. An example of the Xe 6*s* and 6*s*′ Rydberg transitions in the presence of argon is shown in Fig. 2. The primary Xe absorption transition, or [37]

$$\mathrm{Xe} + h\nu \quad \xrightarrow{\mathrm{Ar}} \quad \mathrm{Xe}^*, \tag{23}$$
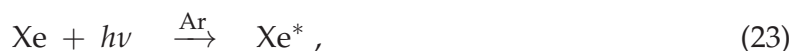
is indicated in Fig. 2 as *a*. The XeAr dimer transitions that yield the blue satellite bands are [22–24]

$$\mathrm{XeAr} + h\nu \quad \xrightarrow{\mathrm{Ar}} \quad \mathrm{Xe}^* + \mathrm{Ar}, \tag{24}$$

and

$$\mathrm{XeAr} + h\nu \quad \xrightarrow{\mathrm{Ar}} \quad \mathrm{Xe}^*\mathrm{Ar}. \tag{25}$$

These transitions are indicated in Fig. 2 as *b* and *c*, respectively.

Detailed investigations [25] of the Xe 6*s* Rydberg state doped in supercritical argon indicated that the energy position at the photoabsorption peak maximum shifted slightly to the red at low argon density and then strongly to the blue (cf. Fig. 3a). Similar results, which are shown in Fig. 3b, were then observed for the Xe 6*s*′ Rydberg states in supercritical argon [26]. These studies [25, 26] concluded that both the perturber-induced energy shift and the line shape broadening were temperature independent. However, since the blue satellite bands grow and broaden as a function of perturber number density, the energy position of the maximum absorption (or the first moment from a moment analysis) is not an accurate energy position for the primary Xe Rydberg transition. Thus, modeling the experimental first moment M_1 and
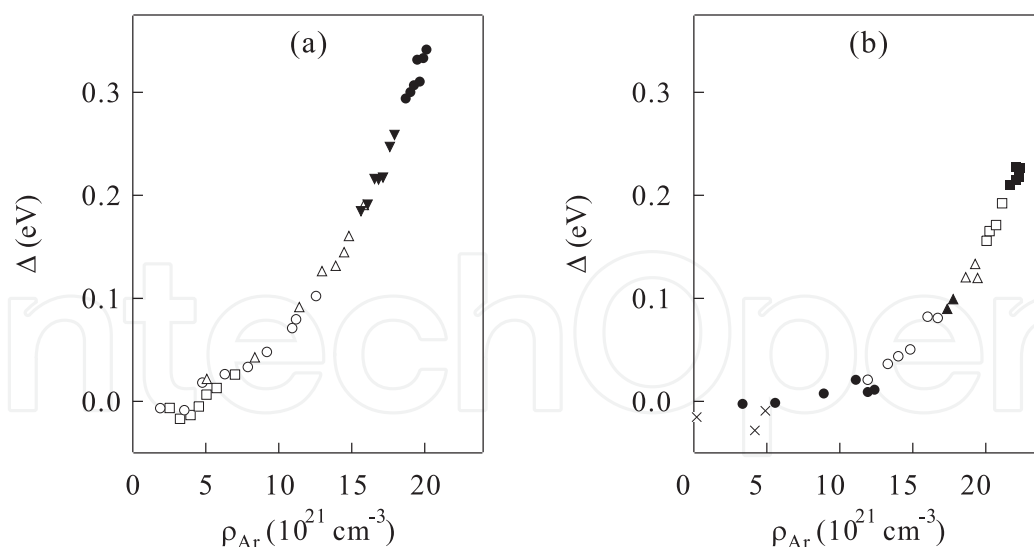
Figure 3. The perturber induced shift Δ of (a) the Xe $6s$ [25] and (b) the Xe $6s'$ [26] absorption maximum plotted as a function of argon number density ρ_{Ar} at different temperatures. In (a), the markers are ($\square$) 25°C; ($\circ$) −83°C; ($\triangle$) −118°C; ($\blacktriangledown$) −138°C; and ($\bullet$) −163°C. In (b), the markers are for temperature ranges of ($\times$) −23°C to 27°C; ($\bullet$) −93°C to −63°C; ($\circ$) −123°C to −113°C; ($\blacktriangle$) −138°C to −128°C; ($\triangle$) −158°C to −148°C; ($\square$) −173°C to −163°C; and ($\blacksquare$) −186°C to −178°C.
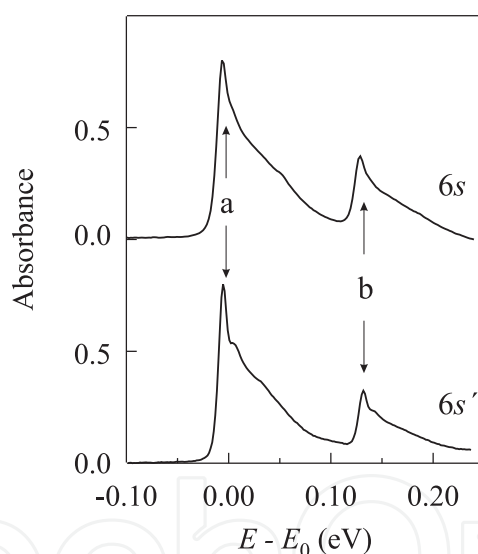

Figure 4. Photoabsorption spectra (relative units) of the CH_3I $6s$ and $6s'$ transitions doped into Ar at an argon number density of $\rho_{Ar} = 1.89 \times 10^{21}$ cm^{-3} and a temperature of −79.8°C. a corresponds to eq. (26) and b to eq. (27). For the $6s$ Rydberg state $E_0 = 6.154$ eV and $E_0 = 6.767$ eV for the $6s'$ Rydberg state. Data from the present work.

second moment M_2 using eqs. (19) and (20) required three groups of intermolecular potential parameters for different perturber density ranges.

The Xe $6s$ and $6s'$ Rydberg transitions [26] in supercritical helium and neon show a similar perturber density dependence as that shown in Fig. 3. However, these two systems do not form ground state or excited state dimers and, therefore, do not have blue satellite bands. Thus, the moment analysis of the photoabsorption spectra presented a more accurate perturber induced shift as a function of perturber number density. Because of the
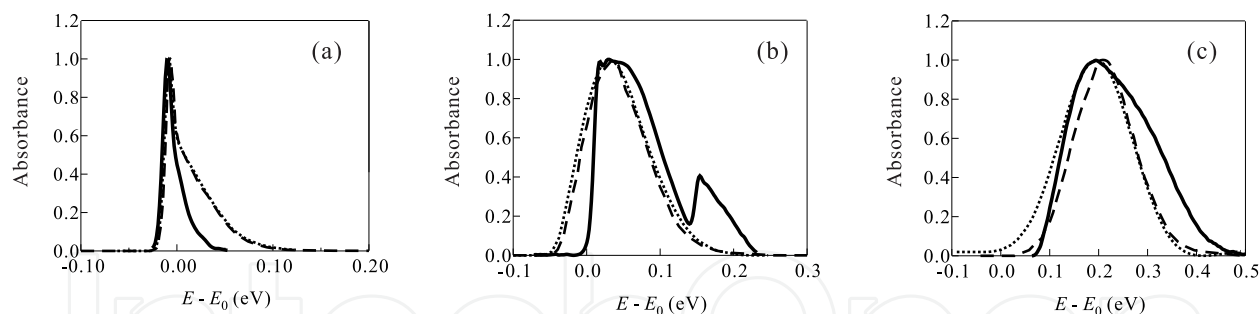
Figure 5. The line shape simulation of the CH_3I $6s$ transition doped into supercritical argon using (- - -) a semi-classical line shape function data [33] and using ($\cdots$) molecular dynamics [32] in comparison to (—) the photoabsorption spectra at (a) $\rho_{Ar} = 2.0 \times 10^{21}$ cm^{-3}, (b) $\rho_{Ar} = 7.6 \times 10^{21}$ cm^{-3}, and (c) $\rho_{Ar} = 2.0 \times 10^{22}$ cm^{-3}. Experimental data are from the present work.

simplicity of the absorption bands, Messing, *et al.* [26] simulated the line shapes of the Xe $6s$ and $6s'$ transitions in both helium and neon at a single perturber number density using eqs. (10) and (11). These simulations indicated that an accurate line shape could be obtained without blue satellite bands [26]. Unfortunately, no temperature dependence was reported in these papers [25, 26].

2.3.2. CH_3I in Ar and Kr

Since CH_3I is a molecular dopant, vibrational transitions as well as the adiabatic transition appear in the photoabsorption spectra. The adiabatic transition is given by [37]

$$CH_3I + h\nu \quad \longrightarrow \quad CH_3I^* , \tag{26}$$

denoted *a* in Fig. 4, as well as one quantum of the CH_3 deformation vibrational transition ν_2 in the excited state, or

$$CH_3I + h\nu \quad \longrightarrow \quad CH_3I^* (\nu_2) , \tag{27}$$
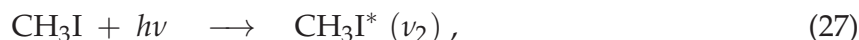
denoted *b*, in Fig. 4.

Although vibrational transitions are apparent, CH_3I [27–29, 32] has been investigated extensively because of the "atomic" like nature of the adiabatic $6s$ and $6s'$ Rydberg transitions. Messing, *et al.* [27, 28] extracted the perturber dependent shift $\Delta(\rho_P)$ of the CH_3I $6s$ and $6s'$ Rydberg states by performing a moment analysis on the photoabsorption bands using eq. (21). This analysis indicated that $\Delta(\rho_P)$ tended first to lower energy and then to higher energy as ρ_P increased from low density to the density of the triple-point liquid, similar to the trends shown in Fig. 3 for Xe in Ar. However, Messing, *et al.* [27, 28] did not explore critical temperature effects on $\Delta(\rho_P)$, nor did they correctly account for the vibrational bands on the blue side of the adiabatic Rydberg transition. Messing, *et al.* [28] did attempt to model the CH_3I $6s$ Rydberg transition in argon using a semi-classical statistical line shape function under the assumption that the adiabatic and vibrational transitions have exactly the same line shapes, although no comparison between the experimental spectra and the simulated line shapes was provided. Later researchers [30–33] concentrated on the simulation of the CH_3I $6s$ Rydberg state doped into argon using both molecular dynamics and semi-classical integral methods. Egorov, *et al.* [33] showed that the semi-classical integral method can yield results comparable to the molecular dynamics calculations of Ziegler, *et al.* [30–32]. Comparing the semi-classical method and molecular dynamics simulation to experimental spectra (cf. Fig. 5) shows that
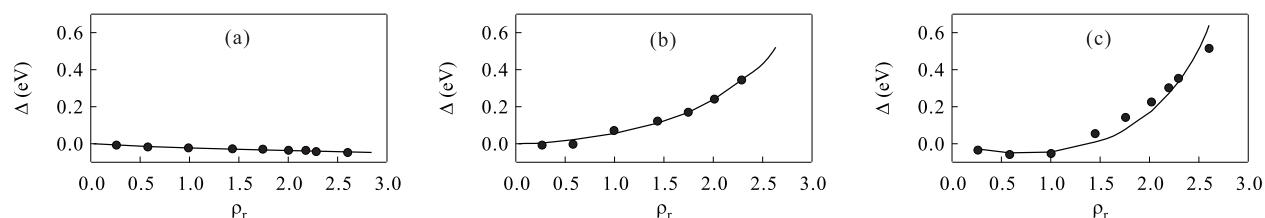
Figure 6. Experimental (●) and calculated (—) energy shift of the NO (a) $B'^2\Delta \leftarrow X^2\Pi$ ($v' = 7, 0$) valence transition, (b) $A^2\Sigma^+ \leftarrow X^2\Pi$ ($v' = 0, 0$) Rydberg transition and (c) $C^2\Pi^+ \leftarrow X^2\Pi$ ($v' = 0, 0$) Rydberg transition plotted versus the reduced argon number density [34].

both methods can be used to simulate the experimental spectra with an appropriate choice of intermolecular potentials.

2.3.3. NO in Ar

Morikawa, *et al.* [34] investigated valence and low-n Rydberg transitions doped into supercritical argon. They used eq. (21) to determine the perturber induced shift $\Delta(\rho_P)$ for several low-n Rydberg transitions as well as a valence transition. Under the assumption of spherically symmetric potentials for the ground and excited states of the NO/Ar systems, an accurate moment analysis using eq. (18) was performed (cf. Fig. 6). In The NO valence state transition (cf. Fig. 6a) shows a slight perturber-induced red shift, which differs significantly from the obvious blue shift of the low-n NO Rydberg state transitions shown in Figs. 6b and c. Fig. 6 also shows that low-n Rydberg states make a more sensitive probe to perturber effects than valence transitions. Later groups [35, 36] did line shape simulations to model the experimental spectra. Larrégaray, *et al.* [35] measured the NO $3s\sigma$ transition doped into supercritical argon at selected argon densities. Then, using molecular dynamics they successfully modeled the line shape of the transition. Once the intermolecular potentials and boundary conditions for the molecular dynamics simulations had been set against experimental data, Larrégaray, *et al.* [35] calculated the line shape for NO in Ar at the critical density and temperature. These calculations predicted that the photoabsorption peak maximum position would shift to the blue when argon was near its critical point. Later, Egorov, *et al.* [36] showed that similar results could be obtained using the semi-classical approximation. Therefore, line shape simulations using molecular dynamics and semi-classical line shape theory show comparable results.

3. Experiment techniques and theoretical methodology

3.1. Experimental techniques

All of the photoabsorption measurements presented in Sections 4 and 5 were obtained using the one-meter aluminum Seya-Namioka (Al-SEYA) beamline on bending magnet 8 of the Aladdin storage ring at the University of Wisconsin Synchrotron Radiation Center (SRC) in Stoughton, WI. This beamline, which was decommissioned during Winter 2007, produced monochromatic synchrotron radiation having a resolution of ~ 8 meV in the energy range of 6 - 11 eV. The monochromatic synchrotron radiation enters the vacuum chamber which is equipped with a sample cell (cf. Fig. 7). The photoabsorption signal is detected by a photomultiplier that is connected to the data collection computer via a Keithley 486 picoammeter. The pressure in the vacuum chamber is maintained at low 10^{-8} to high 10^{-9}
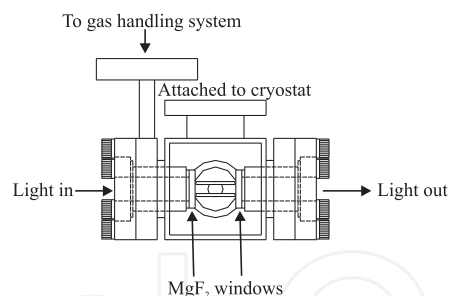
Figure 7. Schematic of the copper experimental cell.

Torr by a Perkin-Elmer ion pump. The experimental copper cell is equipped with entrance and exit MgF_2 windows (with an energy cut-off of 10.9 eV) that are capable of withstanding pressures of up to 100 bar and temperatures of up to 85°C. This cell, which has a path length of 1.0 cm, is connected to an open flow liquid nitrogen cryostat and resistive heater system allowing the temperature to be controlled to within $\pm$ 0.5°C with a Lakeshore 330 Autotuning Temperature controller. The gas sample is added through a gas handling system (GHS), which consists of 316-stainless steel components connected by copper gasket sealed flanges. The initial pressure for the GHS and sample cell is in the low 10^{-8} Torr range.

During the initial bakeout, the GHS and the vacuum chamber were heated to 100°C under vacuum for several days to remove any water adsorbed onto the surface of the stainless steel. The initial bake was stopped when the base pressure of the GHS and sample chamber is in the low 10^{-7} or high 10^{-8} Torr range, so that upon cooling the final GHS base pressure was $10^{-8} - 10^{-9}$ Torr. Anytime a system was changed (either the dopant or the perturber), the GHS was again baked in order to return the system to near the starting base pressure. This prevented cross-contamination between dopant/perturber systems.

The intensity of the synchrotron radiation exiting the monochromator was monitored by recording the beam current of the storage ring as well as the photoemission from a nickel mesh situated prior to the sample cell. The light then entered the experimental cell through a MgF_2 window, traveled through the sample and then a second MgF_2 window (cf. Fig. 7) before striking a thin layer of sodium salicylate powder on the inside of a glass window that preceded the photomultiplier tube. An empty cell (acquired for a base pressure of 10^{-7} or 10^{-8} Torr) spectrum was used to correct the dopant absorption spectra for the monochromator flux, for absorption by the MgF_2 windows, and for any fluctuations in the quantum efficiency of the sodium salicylate window.

Two dopants (i.e. methyl iodide and xenon) and five perturbers (i.e. argon, krypton, xenon, carbon tetrafluoride and methane) were investigated. All dopants and perturbers were used without further purification: methyl iodide (Aldrich, 99.45%), argon (Matheson Gas Products, 99.9999%), krypton (Matheson Gas Products, 99.998%), and xenon (Matheson Gas Products, 99.995%). When CH_3I was the dopant, the CH_3I was degassed with three freeze/pump/thaw cycles prior to use. Photoabsorption spectra for each neat dopant and each neat perturber were measured to verify the absence of impurities in the spectral range of interest. The atomic perturber number densities were calculated from the Strobridge equation of state [55] with the parameters obtained from [56] for argon, [57] for krypton, and [58] for xenon. All densities and temperatures were selected to maintain a single phase system in the sample cell.

At temperatures below T_c, a change in density required a change in temperature, since the isotherms are steeply sloped.

The sensitivity of the absorption spectra to local density required that the quality of a data set be monitored by performing basic data analysis during measurements. Any anomalies were corrected by immediately re-measuring the photoabsorption spectrum for the problem density/temperature/pressure after allowing additional time for increased density stabilization. Once a data set was obtained for non-critical temperatures, the photoabsorption data for perturber densities on an isotherm near the critical isotherm were then measured. For the near critical data set we selected a temperature that was +0.5°C above the critical temperature (chosen to prevent liquid formation in the cell during temperature stabilization near the critical density and to minimize critical opalescence during data acquisition). Near the critical density, the consistency of the density step is dependent on the slope of the critical isotherm. If the critical isotherm has a small slope in this region, it becomes difficult to acquire samples at a constant density step size due to our inability to vary the perturber pressure practically by less than 0.01 bar and to the difficulties encountered in maintaining temperature stability. For instance, near the critical density of xenon, a 1 mbar change in pressure or a 0.001°C change in temperature causes a density change of 2.0×10^{21} cm^{-3}. Maintaining the necessary temperature stability (i.e., $\pm$ 0.2°C) during the acquisition of data along the critical isotherm is difficult with an open flow liquid nitrogen cryostat system and usually required constant monitoring with manual adjustment of the nitrogen flow.

3.2. Theoretical methodology

3.2.1. Line shape function

The experimental line shapes were simulated using the semi-classical statistical line shape function given in eq. (10). Rewriting eq. (10) in terms of the autocorrelation function allows eq. (10) to be given as a Fourier transform, namely [25, 26, 33, 37]

$$\mathfrak{L}(\omega) = \frac{1}{2\pi} \operatorname{Re} \int_{-\infty}^{\infty} dt \, e^{-i\omega t} \left\langle e^{i\omega(\mathbf{R})t} \right\rangle , \tag{28}$$

where $\omega = \omega(\mathbf{R}) - \omega_0$, with ω_0 being the transition frequency for the neat dopant. Eq. (28) neglects lifetime broadening and assumes that the transition dipole moment is independent of $\mathbf{R}$. In the substitution of the exponential density expansion [i.e., eq. (11)] for the autocorrelation function, the general term A_n represents a (n+1)-body interaction [20]. However, since the strength of the interaction decreases as the number of bodies involved increases, and since the higher order interactions are more difficult to model, our line shape simulations are truncated at the second term $A_2(t)$, or three body interactions. Within this approximation, eq. (28) becomes

$$\mathfrak{L}(\omega) = \frac{1}{2\pi} \operatorname{Re} \int_{-\infty}^{\infty} dt \, e^{-i\omega t} \exp\left[A_1(t) + A_2(t)\right] , \tag{29}$$

where the two terms are recalled from eq. (14),

$$A_1(t) = 4\pi\rho_{\mathrm{P}} \int_0^{\infty} dr \, r^2 \, g_{\mathrm{PD}}(r) \left[e^{-it\Delta V(r)} - 1 \right] ,$$

and eq. (15),

$$
\begin{aligned}
A_2(t) = 4\pi \rho_{\rm P}^2 \int_0^\infty dr_1\, r_1^2\, g_{\rm PD}(r_1) \left[{\rm e}^{-it\Delta V(r_1)} - 1 \right] \\
\times \int_0^\infty dr_2\, r_2^2\, g_{\rm PD}(r_2) \left[{\rm e}^{-it\Delta V(r_2)} - 1 \right] \\
\times \frac{1}{r_1\, r_2} \int_{|r_1 - r_2|}^{|r_1 + r_2|} s\, [\, g_{\rm PP}(s) - 1\,]\, ds\, .
\end{aligned}
$$

The required radial distribution functions (i.c., $g_{\rm PP}$ and $g_{\rm PD}$) were obtained from the analytical solution of the Ornstein-Zernike equation for a binary system within the Percus-Yevick (PY) closure [59], while the Fourier transform for eq. (29) was performed using a standard fast Fourier transform algorithm [60]. The line shape obtained from the transform of eq. (29) was convoluted with a standard Gaussian slit function to account for the finite resolution (~ 8 meV) of the monochromator. More detailed discussions are given below.

3.2.2. Fast Fourier transform

A Fourier transform has the general form [60]

$$
F(\omega) = \frac{1}{2\pi} \int_{-\infty}^{\infty} f(t)\, {\rm e}^{-i\omega t}\, dt\, . \tag{30}
$$

Since the line shape function is calculated numerically, the integration limits for eq. (30) must be finite and, therefore, an appropriate integration range must be determined. For any Fourier transformation, the integration limit and the total number of steps are related through [60]

$$
\delta t \times \delta \omega = \frac{2\pi}{N}, \tag{31}
$$

where δ stands for the sampling interval (i.e., the step size) of the corresponding variable and N is the total number of discrete points. Fourier transforms rely on the fact that data are usually obtained in discrete steps and the generating functions $f(t)$ and $F(\omega)$ can be represented by the set of points

$$
\begin{aligned}
f_k \equiv f(t_k)\, , \quad t_k = k\,\delta t\, , \quad k = 1, \dots, N\, , \\
F_n \equiv F(\omega_n)\, , \quad \omega_n = n\,\delta\omega\, , \quad n = -\frac{N}{2}, \dots, \frac{N}{2} - 1\, .
\end{aligned} \tag{32}
$$

Therefore, the function $F(\omega)$ is determined point-wise using

$$
\begin{aligned}
F(\omega_n) &= \frac{1}{2\pi} \int_{-\infty}^{\infty} f(t)\, {\rm e}^{-i\omega_n t}\, dt = \frac{1}{2\pi} \sum_{k=1}^{N} f_k\, {\rm e}^{-i\omega_n t_k}\, \delta t \\
&= \frac{\delta t}{2\pi} \sum_{k=1}^{N} f_k\, {\rm e}^{-i2\pi nk/N}\, .
\end{aligned} \tag{33}
$$

For simplicity, we will define the discrete Fourier transform from time to angular frequency as eq. (33). When computing the Fourier transform from eq. (33), the quickest method is

known as a fast Fourier transform (FFT) and requires that the number of steps N be a power of 2. In our calculations, we use a Cooley-Tukey FFT algorithm [60] with $N = 1024$. The requirements for calculating eq. (30) within this FFT algorithm are, therefore, a complex array of the calculated values of the time dependent autocorrelation function truncated to the second term.

Rewriting eq. (29) using Euler's relation yields [38]

$$\langle e^{i\omega(\mathbf{R})t} \rangle = \text{Re}\langle e^{i\omega(\mathbf{R})t} \rangle + \text{Im}\langle e^{i\omega(\mathbf{R})t} \rangle, \tag{34}$$

where the real and the imaginary parts are given by

$$\text{Re}\langle e^{i\omega(\mathbf{R})t} \rangle = \exp\left[\text{Re}\left(A_1(t) + A_2(t)\right)\right] \cos\left[\text{Im}\left(A_1(t) + A_2(t)\right)\right],$$
$$\text{Im}\langle e^{i\omega(\mathbf{R})t} \rangle = \exp\left[\text{Re}\left(A_1(t) + A_2(t)\right)\right] \sin\left[\text{Im}\left(A_1(t) + A_2(t)\right)\right]. \tag{35}$$

In eq. (35),

$$\text{Re}[A_1(t) + A_2(t)]$$

$$= 4\pi\rho_{\text{P}} \int_0^\infty dr\, r^2\, g_{\text{PD}}(r)\, \left[\cos(\Delta V(r)\, t) - 1\right]$$

$$+ 4\pi\rho_{\text{P}}^2 \int_0^\infty \int_0^\infty dr_1\, dr_2\, h(r_1, r_2)\, \left[\cos(\Delta V(r_1)\, t)\, \cos(\Delta V(r_2)\, t) \right.$$

$$+ 1 - \sin(\Delta V(r_1)\, t)\, \sin(\Delta V(r_2)\, t)$$

$$\left. - \cos(\Delta V(r_1)\, t) - \cos(\Delta V(r_2)\, t)\right], \tag{36}$$

and

$$\text{Im}[A_1(t) + A_2(t)]$$

$$= -4\pi\rho_{\text{P}} \int_0^\infty dr\, r^2\, g_{\text{PD}}(r)\, \left[\sin(\Delta V(r)\, t)\right]$$

$$- 4\pi\rho_{\text{P}}^2 \int_0^\infty \int_0^\infty dr_1\, dr_2\, h(r_1, r_2)\, \left[\sin(\Delta V(r_1)\, t)\, \cos(\Delta V(r_2)\, t) \right.$$

$$+ \cos(\Delta V(r_1)\, t)\, \sin(\Delta V(r_2)\, t)$$

$$\left. - \sin(\Delta V(r_1)\, t) - \sin(\Delta V(r_2)\, t)\right], \tag{37}$$

with

$$h(r_1, r_2) = r_1\, g_{\text{PD}}(r_1)\, r_2\, g_{\text{PD}}(r_2) \int_{|r_1 - r_2|}^{|r_1 + r_2|} s\, [g_{\text{PP}}(s) - 1]\, ds.$$

The output of the FFT is a complex function of frequency. The real portion of this complex function is obtained and then convoluted with a standard Gaussian slit function. The final output is the simulated line shape function. Since eqs. (29), (36) and (37) depend on both the radial distribution functions and the ground-state and excited-state intermolecular potentials, these are discussed in more detail below.

3.2.3. Radial distribution function

After significant investigation, we found that the most stable calculation technique for obtaining radial distribution functions for this problem was the analytical solution of the Ornstein-Zernike relation within the Percus-Yevick (PY) closure [59]. Although this solution for a binary system yields four coupled integro-differential equations, dilute solutions (i.e., $\rho_D \ll \rho_P$) allows these equations to be reduced to the calculation of the perturber/dopant radial distribution function $g_{PD}(r)$ and the perturber/perturber radial distribution function $g_{PP}(r)$. This solution is given by [12, 59]

$$
\begin{aligned}
g_{PD}(r) &= r^{-1} e^{-\beta V_g(r)} Y_{PD}(r) \\
g_{PP}(r) &= r^{-1} e^{-\beta V_g'(r)} Y_{PP}(r) ,
\end{aligned}
\tag{38}
$$

where

$$
\begin{aligned}
Y_{PD}(r) &= \int_0^r dt \; \frac{dY_{PD}(t)}{dt} , \\[2mm]
Y_{PP}(r) &= \int_0^r dt \; \frac{dY_{PP}(t)}{dt} ,
\end{aligned}
\tag{39}
$$

with

$$
\begin{aligned}
\frac{d}{dr} Y_{PD}(r) = 1 &+ 2\pi\rho_P \int_0^\infty dt \left(e^{-\beta V_g(t)} - 1 \right) Y_{PD}(t) \\
&\times \left[e^{-\beta V_g'(r+t)} Y_{PP}(r+t) \right. \\
&\quad \left. - \frac{r-t}{|r-t|} e^{-\beta V_g'(|r-t|)} Y_{PP}(|r-t|) - 2t \right] ,
\end{aligned}
\tag{40}
$$

$$
\begin{aligned}
\frac{d}{dr} Y_{PP}(r) = 1 &+ 2\pi\rho_P \int_0^\infty dt \left(e^{-\beta V_g'(t)} - 1 \right) Y_{PP}(t) \\
&\times \left[e^{-\beta V_g'(r+t)} Y_{PP}(r+t) \right. \\
&\quad \left. - \frac{r-t}{|r-t|} e^{-\beta V_g'(|r-t|)} Y_{PP}(|r-t|) - 2t \right] ,
\end{aligned}
$$

and with V_g and V_g' being the ground state perturber/dopant and ground state perturber/perturber intermolecular potentials, respectively.

3.2.4. Intermolecular potentials

Eqs. (29), (34) - (40) are explicitly dependent on the excited-state and ground-state perturber/dopant intermolecular potentials through $\Delta V(r)$, and are implicitly dependent

on the perturber/perturber and perturber/dopant ground-state intermolecular potential via $g_{PP}(r)$ and $g_{PD}(r)$. Thus, these simulations require one to develop a single set of ground-state and excited-state intermolecular potential parameters for each system. A standard Lennard-Jones 6-12 potential, or

$$V(r) \;=\; 4\varepsilon \left[\left(\frac{\sigma}{r} \right)^{12} - \left(\frac{\sigma}{r} \right)^{6} \right], \tag{41}$$

was chosen for the atomic perturber/perturber ground-state intermolecular interactions, and non-polar dopant/perturber ground-state intermolecular interactions. The ground-state molecular perturber/perturber intermolecular potential was a two-Yukawa potential, or

$$V(r) \;=\; -\frac{\kappa_0\,\varepsilon}{r} \left[e^{-z_1(r-\sigma)} - e^{-z_2(r-\sigma)} \right]. \tag{42}$$

The ground-state polar dopant/perturber intermolecular interactions were modeled using a modified Stockmeyer potential

$$V(r) \;=\; 4\varepsilon' \left[\left(\frac{\sigma'}{r} \right)^{12} - \left(\frac{\sigma'}{r} \right)^{6} \right] - \frac{1}{r^6}\alpha_P \mu_D^2, \tag{43}$$

which can be rewritten in standard Lennard-Jones 6-12 potential form [12], with

$$\varepsilon \;=\; \varepsilon' \left[1 + \frac{\alpha_P\,\mu_D^2}{4\,\varepsilon'\,\sigma'^6} \right]^2,$$

$$\sigma \;=\; \sigma' \left[1 + \frac{\alpha_P\,\mu_D^2}{4\,\varepsilon'\,\sigma'^6} \right]^{-1/6}.$$

(The modified Stockmeyer potential includes orientational effects via an angle average that presumes the free rotation of the polar dopant molecule.) An exponential-6 potential, given by

$$V(r) \;=\; \frac{\varepsilon}{1 - (6/\gamma)} \left\{ \frac{6}{\gamma}\, e^{\gamma(1-\chi)} - \chi^{-6} \right\}, \tag{44}$$

was chosen for the excited-state dopant/ground-state perturber interactions. In eqs. (41) - (44), ε is the well depth, σ is the collision parameter, α_P is the perturber polarizability, μ_D is dopant dipole moment, $\chi \equiv r/r_e$ (where r_e is the equilibrium distance), and γ is the potential steepness.

The Lennard-Jones parameters for the atomic fluids and the modified Stockmeyer parameters for the CH_3I/Ar and CH_3I/Kr interactions were identical to the parameters used to model accurately the perturber-induced shift of the dopant ionization energy for methyl iodide in argon [12–14, 61], krypton [12, 15, 61] and xenon [16, 61]. The parameters κ_0, z_1, z_2, ε and σ in eq. (42) were adjusted to give the best fit to the phase diagram of the perturber [61]. The parameters ε, σ, χ and γ in eq. (44) were adjusted by hand to give the "best" fit to the experimental absorption spectra of the dopant low-n Rydberg states in each of the fluids investigated here.
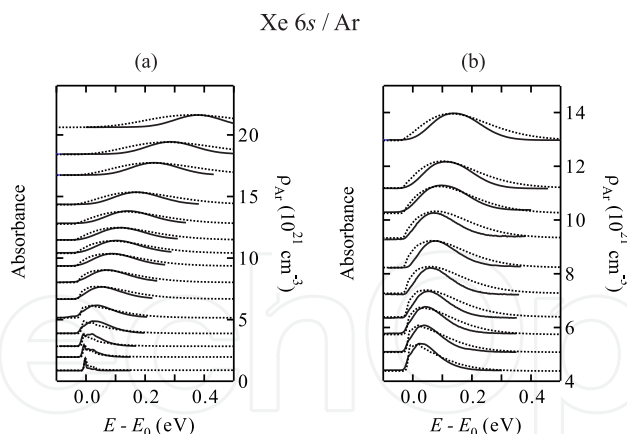
Xe 6*s* / Ar

Figure 8. Selected photoabsorption spectra (–, relative scale) and simulated line shapes (· · ·) for the Xe 6*s* Rydberg transitions at (a) non-critical temperatures and (b) on an isotherm (i.e., $-121.8°$C) near the critical isotherm. The data are offset vertically by the argon number density ρ_{Ar}. The transition energy is $E_0 = 8.424$ eV for the unperturbed Xe 6*s* Rydberg transition.

4. Atomic perturbers

4.1. Xe low-*n* Rydberg states in Ar

4.1.1. Xe absorption

The Xe 6*s* and 6*s'* Rydberg states (where *s* and *s'* denote the $J = 3/2$ and $J = 1/2$ angular momentum core state, respectively) were experimentally measured in dense argon. As is discussed in Section 2.4.1, when Xe interacts with Ar, ground and excited state dimers form. These dimers are evidenced by blue satellite bands that arise on the higher energy side of the primary Rydberg transition. The Xe 6*s* Rydberg transition has two such blue satellite bands corresponding to eqs. (24)-(25), whereas the Xe 6*s'* Rydberg transition has a single blue satellite band corresponding to eq. (24) (cf. Fig. 2) [22–24]. The absence of the ground state XeAr dimer to XeAr eximer transition [i.e., eq. (25)] for the Xe 6*s'* Rydberg state may be caused by an extremely short lifetime preventing our ability to detect the transition or by the XeAr eximer decomposing during the excitation.

The solid lines in Fig. 8 present selected experimental Xe 6*s* Rydberg transitions doped into supercrtical argon at non-critical temperatures and along an isotherm near the critical isotherm offset by the argon number density. (Similar data for the Xe 6*s'* Rydberg transitions are not shown for brevity.) It can be clearly seen that the Rydberg transitions broaden as a function of the argon number density. The maximum of the absorption band also shifts first slightly to the red and then strongly to the blue, similar to the original observations of Messing, *et al.* [25, 26]. Since the ground state interaction between Xe and Ar (or XeAr and Ar) is attractive, the ground states are stabilized by the argon solvent shell. The slight red shift observed at low argon number densities indicates that the xenon excited states (either Xe* or Xe*Ar) are also stabilized by the argon solvent shell. As the density increases, however, argon begins to shield the optical electron from the xenon cationic core, thereby decreasing the binding energy of the optical electron . Thus, as the density of argon increases the energy of the excited state also increases, leading to a blue shift in the transition energy at higher densities. Although not shown, the overall blue shift of the 6*s* Rydberg transition band is much larger than that of the 6*s'* band at the triple point liquid density of argon. This difference

in overall shift is caused by the difference in the core state of the cation, since the $J = 1/2$ core state has a permanent quadrupole moment. This permanent quadrupole moment increases the interaction of the cationic core and the optical electron, thereby implying that the optical electron is less perturbed by the argon solvent shell.

However, since the blue satellite bands also broaden and shift with increasing argon density, the primary Xe transition becomes indistinguishable at medium to large argon number densities. Thus, the argon-induced energy shift of the primary Xe transition cannot be investigated directly using these data. Therefore, to probe perturber critical effects on the dopant excited states, we must first accurately simulate the absorption spectra over the entire argon density range at non-critical temperatures and on an isotherm near the critical isotherm.

4.1.2. Discussion

In order to simulate accurately the absorption spectra at high density, any line shape simulation has to include the primary transition, denoted a in Fig. 2 and given by eq. (23), as well as the two XeAr dimer transitions that yield the blue satellite bands, denoted b and c in Fig. 2 and given by eqs. (24) and (25), respectively. For the simulation of Xe in Ar, we chose to use eq. (41) for the ground state Ar/Ar, Xe/Ar, and XeAr/Ar interactions and eq. (44) for the Xe*/Ar and Xe*Ar/Ar interactions. We also required that the simulation use a single set of intermolecular potential parameters for the entire argon density range at non-critical temperatures and along the critical isotherm. All intermolecular potential parameters except the Ar/Ar ground state parameters were adjusted by hand to give the best simulated line shape in comparison to the experimental data. The values of these parameters are given here in Appendix A [37, 40].

The relative intensities of the simulated bands were set by comparison to the absorption spectra of Xe doped into argon at argon number densities where all bands could be clearly identified. Experimentally, at low argon number densities, the ratio of heights between the b band and the primary transition is 0.2 for both the Xe $6s$ and $6s'$ Rydberg states in Ar. For the Xe $6s$ Rydberg state in Ar, the ratio of heights between the c band and the primary transition is 0.45. Although for concentrated Xe systems, the ratio of heights for the blue satellite bands to the primary transition would increase with decreasing temperature or increasing perturber number density, this is not the case for the very dilute Xe/Ar system investigated here (i.e., [Xe] < 10 ppm for all argon number densities). Therefore, we can assume that the intensity ratio of the blue satellite bands to the primary transitions stays constant at different temperatures and different argon densities.

The dotted lines in Fig. 8 are the simulated line shapes for the Xe $6s$ transition at non-critical temperatures (cf. Fig. 8a) and on an isotherm ($-121.8°C$) near the critical isotherm (cf. Fig. 8b). A similar figure for the Xe $6s'$ transition is not shown for brevity. Clearly, the simulated spectra closely match the experimental spectra for all densities. Both the simulated and experimental line shapes show a slight red shift at low argon number densities, followed by a strong blue shift at high argon number densities. With these accurate line shape simulations, moment analyses can be performed on the primary transition in order to investigate perturber critical point effects, as well as to discuss trends in solvation of different dopant electronic transitions in the same simple atomic fluid.
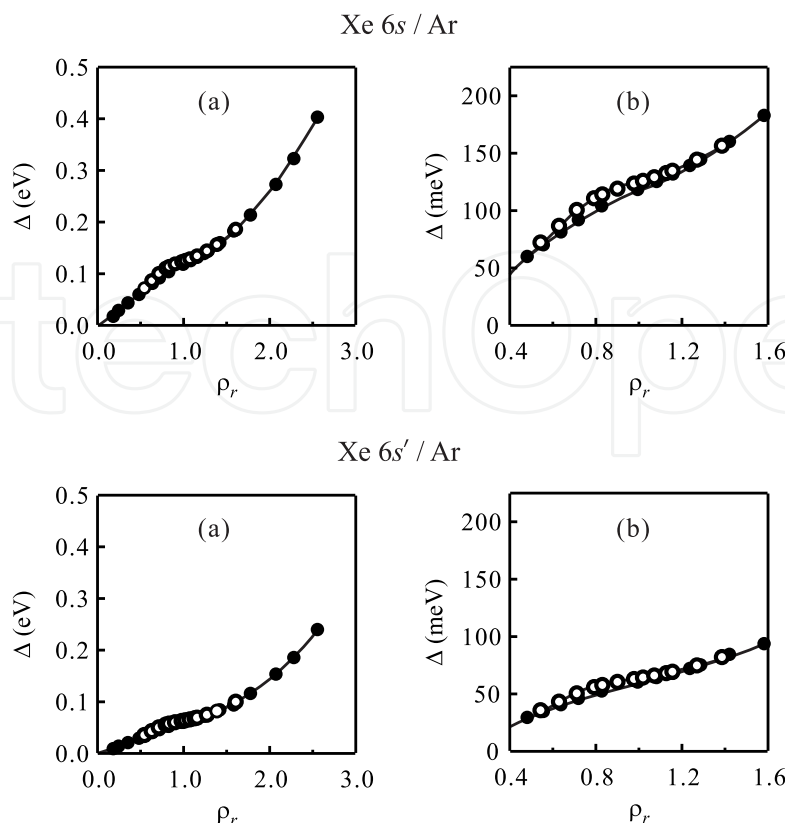
Figure 9. (a) The argon induced shift $\Delta(\rho_{Ar})$, as approximated by eq. (21), of the primary transition for the Xe 6*s* and 6*s'* Rydberg states as a function of argon number density ρ_{Ar} at (•) non-critical temperatures and (○) along an isotherm near the critical isotherm. (b) An expanded view of $\Delta(\rho_{Ar})$ The solid lines are a visual aid. See text for discussion.

A line shape analysis was performed on the accurate simulations of the primary Xe 6*s* and 6*s'* Rydberg transitions in order to determine the average argon induced shift $\Delta(\rho_{Ar})$ of the primary transition, as approximated from the first moment [i.e., eq. (21)]. This moment analysis is shown in Fig 9 as a function of reduced argon number density ρ_r, where $\rho_r = \rho_{Ar}/\rho_c$ with $\rho_c \equiv 8.076 \times 10^{21}$ cm^{-3} [56]. Fig 9b shows an enhanced view of the perturber critical region with a critical effect in $\Delta(\rho_{Ar})$ clearly apparent. The absence of the red shift observed by Messing, *et al.* [25, 26] (cf. Fig. 3) results from our performance of a moment analysis on a blue degraded band, instead of a direct non-linear least square analysis using a Gaussian fit function on the primary transition. In other words, while the peak of the primary transition red shifts slightly at low argon densities, the first moment of the band does not, due to the perturber induced broadening.

General trends emerged in the behavior of the simulated line shape as a function of the intermolecular potential parameters. For instance, we observed that the strength of the asymmetric blue broadening of a band increases with increasing $\Delta r_e \equiv r_e^{(g)} - r_e^{(e)}$ [where $r_e^{(i)}$ is the equilibrium dopant/perturber distance for either the ground state dopant ($i = g$) or the excited state dopant ($i = e$)]. However, the overall perturber-induced energy shift of the band depended on the ground state intermolecular potential well depth $\varepsilon^{(g)}$ as well as Δr_e. The slight red shift at low perturber number densities, however, was controlled by the excited state intermolecular potential well depth $\varepsilon^{(e)}$. Comparison of the Xe 6*s* and 6*s'* transition in Ar

shows that the 6s Rydberg state broadens and shifts to higher energies more quickly than does the 6s' state. Since both transitions are excited from the same ground state (implying that the ground state intermolecular potential parameters remain unchanged), Δr_e must decrease and $\varepsilon^{(e)}$ increase in order to simulate the Xe 6s' Rydberg state in argon correctly. These general trends proved helpful when determining the intermolecular potential parameters for new systems.

Messing, *et al.* [25, 26] concluded that the argon induced energy shift is density dependent and temperature independent. However, both our experimental absorption spectra and the line shape simulations show a distinct temperature dependence near the argon critical point. To test the sensitivity of the perturber critical point effect, we extracted the perturber dependent shift $\Delta(\rho_{Ar})$ of the simulated primary Xe 6s transition in supercritical argon near the critical density along three different isotherms (i.e., $T_r = 1.01$, 1.06 and 1.11, where $T_r = T/T_c$ with $T_c = -122.3°C$). These data are shown in Fig. 10a and clearly indicate that the critical effect is extremely sensitive to temperature and can be easily missed if the temperature of the system is not maintained close to the critical isotherm.
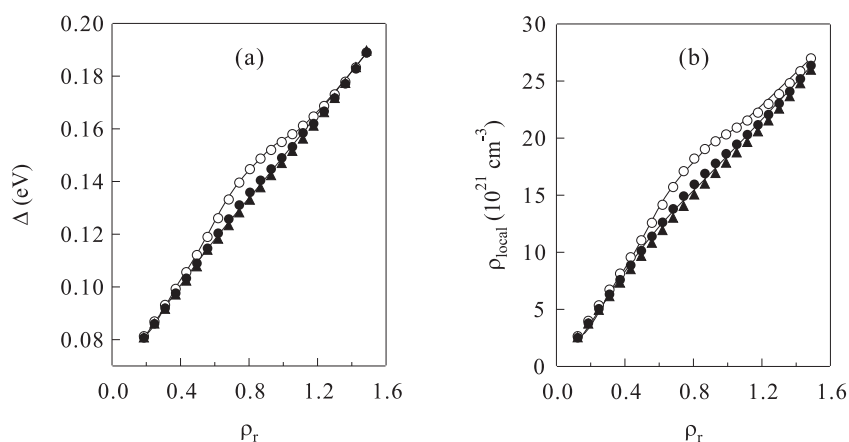

Figure 10. (a) The calculated argon induced shift $\Delta(\rho_{Ar})$ doped into supercritical argon plotted as a function of reduced argon number density at a reduced temperature $T_r = 1.01$ (○), 1.06 (●) and 1.11 (▲). (b) The local densities ($\rho_{local} = g_{max}\rho_{bulk}$) of the first argon solvent shell around a central Xe atom plotted as a function of reduced argon number density at a reduced temperature $T_r \simeq 1.01$ (○), 1.06 (●) and 1.11 (▲). The solid lines are provided as visual aid.

If we return to the line shape equation [i.e., eq. (29)], we observe that the two-body interaction term $A_1(t)$ and the three-body interaction term $A_2(t)$ depend on the difference between the excited state and ground state intermolecular potentials and on the perturber/dopant radial distribution function. Since the potential difference will not depend dramatically on temperature, the critical point effect must be dominated by changes in the perturber/dopant radial distribution function $g_{PD}(r)$. In Fig. 10b, we plot the local density of the first solvent shell as a function of the bulk reduced argon number density on the same three isotherms. The $T_r = 1.01$ isotherm shows a much larger density deviation near the critical density in comparison to the other two isotherms. Thus, the argon induced blue shift is caused by the first perturber shell shielding the cationic core from the optical election. This increase in shielding decreases the binding energy of the electron, thereby increasing the excitation energy.

4.2. CH$_3$I low-*n* Rydberg states in Ar, Kr and Xe

4.2.1. CH$_3$I absorption

The CH$_3$I 6*s* and 6*s*′ Rydberg states doped into supercritical argon, krypton and xenon were investigated both experimentally and theoretically [38, 40] from low perturber number density to the density of the triple point liquid, at both non-critical temperatures and on an isotherm near (i.e., +0.5°C) the critical isotherm of the perturber. The CH$_3$I 6*s* and 6*s*′ Rydberg states show perturber-induced energy shifts and broadening similar to that observed for the Xe low-*n* Rydberg states in supercritical argon. The peak positions of the absorption spectra shift to the red slightly and then strongly to the blue as a function of perturber number densities. This is similar to the behavior for CH$_3$I in dense rare gases observed by Messing, *et al.* [27, 28]. Unlike Xe, which forms heterogenous dimers in argon, the CH$_3$I/perturber interactions are weaker. Thus, CH$_3$I does not possess blue satellite bands caused by dimer or excimer formation. However, CH$_3$I does possess a strong vibrational transition on the blue side of the adiabatic transition. Fig. 4 shows the absorption of both the 6*s* and 6*s*′ Rydberg states of CH$_3$I and clearly illustrates the vibrational state, which represents the CH$_3$ group deformation vibrational band ν_2. The solid lines in Figs. 11 - 13 represent selected photoabsorption spectra for the CH$_3$I 6*s* Rydberg transition doped into supercrtical argon, krypton and xenon, while similar plots for the CH$_3$I 6*s*′ transition are not shown for brevity. Experimental spectra of CH$_3$I in Xe at number densities between 5.0×10^{21} cm^{-3} and 7.0×10^{21} cm^{-3} could not be obtained, because of the large density deviation induced by small temperature fluctuations ($\approx 2.0 \times 10^{21}$ cm^{-3} for a 0.001°C temperature change) in this density region.

The experimental absorption of CH$_3$I low-*n* Rydberg transitions shows that as the perturber number density increases, the ν_2 vibrational band broadens and shifts until it merges with the adiabatic transition. Therefore, determining the perturber induced shift $\Delta(\rho_P)$ of the adiabatic transition from a simple moment analysis of the spectra presented in Figs. 11 - 13 is not possible, and we must perform an accurate line shape analysis of these data in order to extract $\Delta(\rho_P)$ and investigate the perturber critical effect. However, some qualitative information can be gleaned from Figs. 11 - 13. First, the rate of the broadening and the rate of shift for both the adiabatic transition band and the ν_2 vibrational transition band differ dramatically for different perturbers. However, although not shown, the CH$_3$I 6*s* and 6*s*′ transitions have almost the same perturber induced shift, which differs from the behavior observed for the Xe in Ar system previously presented.

4.2.2. Discussion

Although CH$_3$I in the rare gases does not form dimers or excimers, the accurate simulation of the low-*n* Rydberg transitions must include both the adiabatic transition, given by eq. (26) and denoted *a* in Fig. 4, as well as one quantum of the CH$_3$ deformation vibrational transition ν_2 in the excited state, given by eq. (27) and denoted *b* in Fig. 4. For all of the simulations presented here, we again chose eq. (41) for the ground-state perturber/perturber intermolecular interactions. All of the ground-state dopant/perturber interactions, on the other hand, were approximated with eq. (43). The excited-state dopant/ground state perturber interactions were again modeled using eq. (44). All intermolecular potential parameters except the Ar/Ar, Kr/Kr, Xe/Xe, CH$_3$I/Ar, and CH$_3$I/Kr ground state potential parameters were adjusted by hand to give the best simulated line shape in comparison to

our experimental absorption spectra. (The Ar/Ar, Kr/Kr, Xe/Xe, CH$_3$I/Ar, and CH$_3$I/Kr ground-state potential parameters used are in accord with those employed in our earlier studies of the quasi-free electron energy in rare gas perturbers [12].) Appendix A gives the values for all intermolecular potential parameters used in the line shape simulations presented here. The relative intensities of the simulated bands were fixed by comparison to the absorption spectra of CH$_3$I at perturber number densities where all bands (i.e., the adiabatic and vibrational transitions) could be clearly identified. Experimentally, at low perturber number densities the ratio of the vibrational band intensity to the adiabatic transition intensity is 0.22 for both the CH$_3$I $6s$ and $6s'$ Rydberg states in all three perturbers.
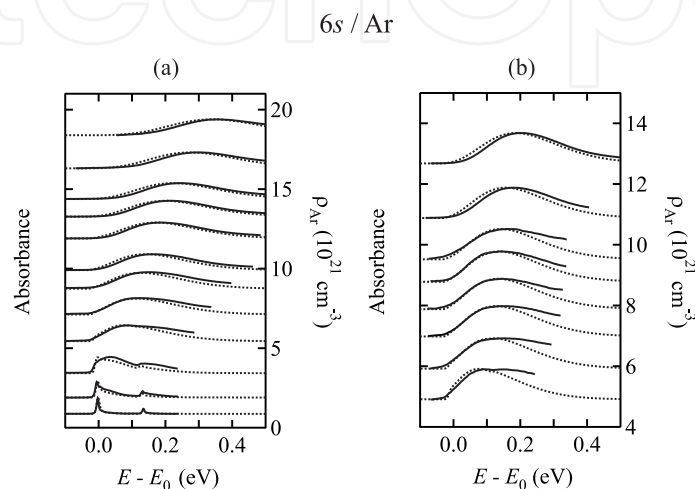
$6s$ / Ar

Figure 11. Selected photoabsorption spectra (—, relative units) and simulated line shapes ($\cdots$) for the CH$_3$I $6s$ Rydberg transition in argon at (a) non-critical temperatures and (b) on an isotherm ($-121.8°$C) near the critical isotherm. The data are offset vertically by the argon number density ρ_{Ar}. The transition energy is $E_0 = 6.154$ eV for the unperturbed CH$_3$I $6s$ Rydberg transition. The variation between experiment and simulation is caused by other vibrational transitions and by perturber-dependent lifetime broadening not modeled here.

The dotted lines in Figs.11 - 13 present the simulated line shapes (dotted lines) of the low-n CH$_3$I Rydberg transitions in the atomic perturbers at non-critical temperatures and on an isotherm near the critical isotherm of the perturber. As was true for Xe in Ar, the simulated spectra closely match the experimental spectra for all densities. Both the simulated and experimental line shapes show a slight red shift at low perturber number densities, followed by a strong blue shift at high perturber densities. Given the accuracy of the simulated line shapes, simulated spectra for CH$_3$I in Xe in the region where experimental data were unobtainable are also presented in Fig. 13. We should note here that we were able to model the CH$_3$I $6s$ and $6s'$ Rydberg states in Ar using the same set of intermolecular potential parameters for both states. This behavior was also observed for the CH$_3$I $6s$ and $6s'$ Rydberg states in Kr. With identical potential parameters, the perturber induced shift $\Delta(\rho_{\text{P}})$ will be the same for the $6s$ and $6s'$ states. The independence of $\Delta(\rho_{\text{P}})$ on the dopant cationic core state is different from that observed for Xe low-n Rydberg states in Ar and will be discussed in more detail below. The accurate line shape simulations allow $\Delta(\rho_{\text{P}})$ for the adiabatic transitions to be extracted using eq. (21).

As with Xe in Ar, the accurate line shape simulations allow a moment analysis to be performed on the CH$_3$I low-n adiabatic Rydberg transition to obtain the perturber induced shift $\Delta(\rho_{\text{P}})$
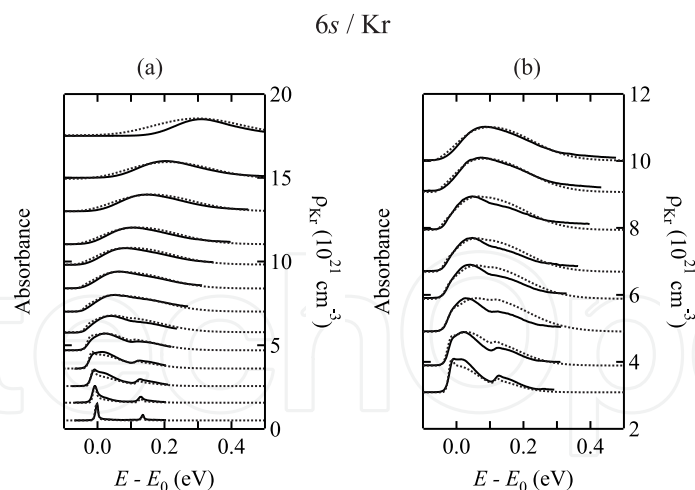
6*s* / Kr

Figure 12. Selected photoabsorption spectra (—, relative units) and simulated line shapes (· · ·) for the CH₃I 6*s* Rydberg transition in krypton at (a) non-critical temperatures and (b) on an isotherm (−63.3°C) near the critical isotherm. The data are offset vertically by the krypton number density ρ_{Kr}. The transition energy is $E_0 = 6.154$ eV for the unperturbed CH₃I 6*s* Rydberg transition. The variation between experiment and simulation is caused by other vibrational transitions and by perturber-dependent lifetime broadening not modeled here.

6*s* / Xe
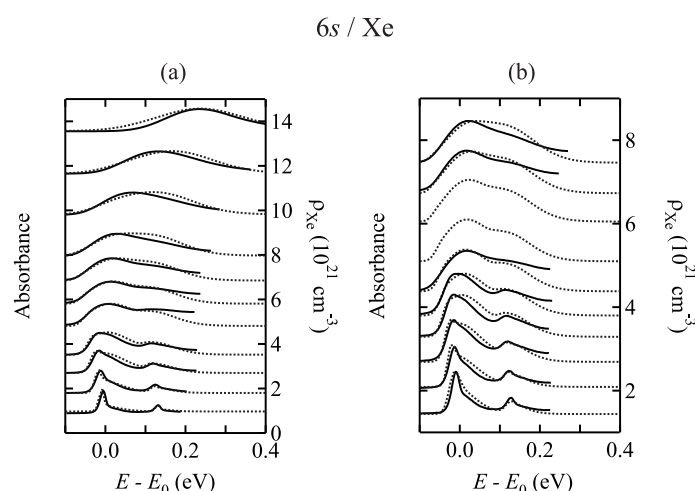
Figure 13. Selected photoabsorption spectra (—, relative units) and simulated line shapes (· · ·) for the CH₃I 6*s* Rydberg transition in xenon at (a) non-critical temperatures and (b) on an isotherm (17.0°C) near the critical isotherm. The data are offset vertically by the xenon number density ρ_{Xe}. The transition energy is $E_0 = 6.154$ eV for the unperturbed CH₃I 6*s* Rydberg transition. The variation between experiment and simulation is caused by other vibrational transitions and by perturber-dependent lifetime broadening not modeled here.

from eq.(21). The first moment of the simulated CH₃I 6*s* adiabatic transition is plotted as a function of the reduced perturber number density ρ_r in Fig. 14 for the 6*s* transition. (A similar figure for the 6*s*′ transition is not shown for brevity.) The first moment of the simulated adiabatic band does not red shift at low perturber density, as was originally stated by Messing, *et al.* [27, 28]. This absence of a red shift is again caused by the blue degradation of the adiabatic transition, which places the average energy (i.e., the first moment) of the band to the high energy side of the absorption maximum. The ground state interaction between CH₃I and the perturber is attractive, and therefore the ground state of the dopant is stabilized by

the perturber solvent shell. The slight red shift of the absorption maximum observed at low perturber number densities is indicative of the stabilization of the CH_3I excited states by the perturber solvent shell. As the density increases, however, perturber molecules begin to shield the optical electron from the CH_3I cationic core, thereby increasing the excitation energy of the optical electron. Thus, as the perturber density increases, the energy of the excited state also increases, leading to a blue shift at higher perturber densities.

The $6s$ and $6s'$ Rydberg states correspond to an optical electron in the same Rydberg orbital, but with the cation in a different core state: $J = 3/2$ for s and $J = 1/2$ for s', where J is the total angular momentum of the core. In our investigation of $\Delta(\rho_P)$ for Xe in Ar, we found that $\Delta(\rho_P)$ of the $6s$ transition is 0.2 eV larger than that for the $6s'$ transition, indicating that the change in the core quadrupole moment affects the dopant/perturber interactions in a dense perturbing medium. However, $\Delta(\rho_P)$ for the CH_3I $6s$ and $6s'$ Rydberg transitions near the triple point density are identical to within experimental error for the perturbers argon and krypton, and differ only slightly (i.e., 30 meV) for CH_3I in xenon. The insensitivity of these CH_3I/perturber systems to the change in the CH_3I cationic core is probably caused by the large permanent dipole moment of CH_3I, which masks the effect of the quadrupole moment. Xenon, however, is extremely sensitive to electric fields because of its large polarizability. Therefore, the slight difference between the xenon induced shifts of the CH_3I $6s$ and $6s'$ Rydberg transitions may well be caused by small changes in the permanent dipole moment of CH_3I influencing changes in the induced dipole or local quadrupoles in the xenon perturber.

A critical point effect on the $6s$ and $6s'$ transition energies is also apparent in Fig. 14 for all three perturbers. The CH_3I $6s$ adiabatic transition in argon is blue-shifted by 20 meV near the critical temperature and critical density, while those in krypton and xenon are blue-shifted by 30 meV and 15 meV, respectively. Identical results are obtained for the CH_3I $6s'$ adiabatic transitions in argon and krypton. However, a smaller critical effect of 5 meV is observed for the CH_3I $6s'$ transition in xenon, which is related to the smaller overall blue shift of the CH_3I $6s'$ transition in comparison to the $6s$ transition.

In the low to medium density range, the energy of the absorption maximum for the $6s$ and $6s'$ CH_3I Rydberg states has a larger red shift in xenon, which is caused by the larger xenon polarizability. The CH_3I Rydberg states also broaden more quickly in xenon. This increased broadening is probably due to a combination of increased xenon polarizability and an increase in the probability of collisional de-excitation due to the size of xenon. However, $\Delta(\rho_P)$ is larger for argon than for krypton and xenon. This change is caused by an overall decrease in the total number of perturber atoms within the first solvent shell surrounding the CH_3I dopant as the perturber atoms become larger. The variation in the critical point effect, with krypton having a larger effect than argon and xenon, is caused by the strength of the perturber/CH_3I interactions in comparison to the perturber/perturber interactions, coupled with the differences in the ground-state and excited-state dopant/perturber interaction potentials. The CH_3I/Kr ground state potential well depth is close (i.e., 24 K) to the Kr/Kr potential well depth. This implies that the CH_3I/Kr interactions near the krypton critical point will be comparable to the Kr/Kr interactions, thereby leading to a large increase in the local perturber density near the critical point of the perturber, and a larger critical point effect. Similarly, the critical point effect decreases as one goes from krypton to argon to xenon because the difference in well depth for all intermolecular potentials increases.
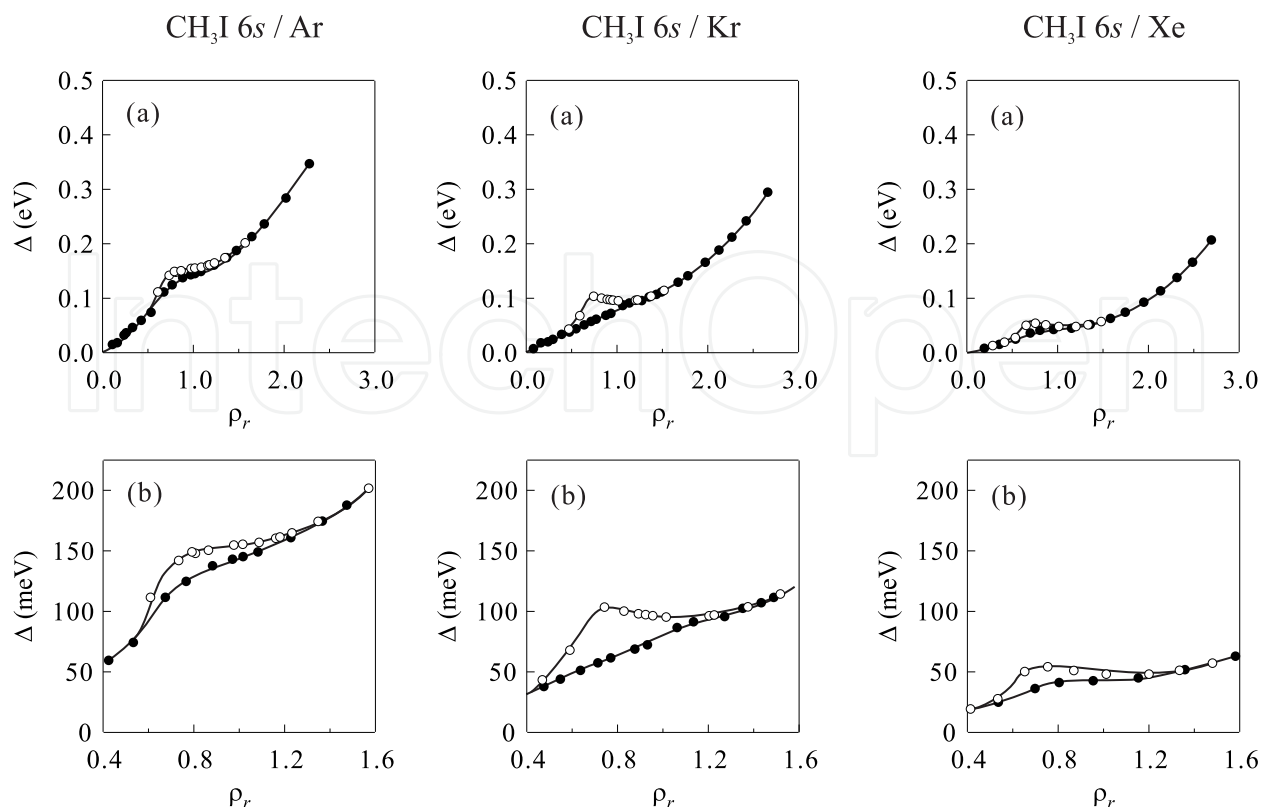
CH₃I 6*s* / Ar   CH₃I 6*s* / Kr   CH₃I 6*s* / Xe

Figure 14. (a) The perturber induced shift $\Delta(\rho_P)$, as approximated by a moment analysis [i.e., eq. (21)], of the simulated primary transition for the CH₃I 6*s* Rydberg state as a function of the reduced perturber number density ρ_r for argon, krypton and xenon. (●), simulations obtained at noncritical temperatures; (○), simulations near the critical isotherm. (b) An expanded view of $\Delta(\rho_P)$ near the perturber critical point. $\rho_c = 8.0 \times 10^{21}$ cm^{-3} for argon, $\rho_c = 6.6 \times 10^{21}$ cm^{-3} for krypton and $\rho_c = 5.0 \times 10^{21}$ cm^{-3} for xenon [12]. The solid lines provide a visual aid. See text for discussion.

5. Conclusion

In this work, the structure of low-*n* Rydberg states doped into supercritical fluids was investigated in several atomic perturbers. Both the experimental absorption spectra and full line shape simulations over the entire perturber density range at non-critical temperatures and along isotherms near perturber critical isotherms were presented for all dopant/perturber systems. These accurate line shape simulations allowed us to extract the perturber-induced energy shift $\Delta(\rho_P)$ from the simulated primary low-*n* Rydberg transitions. These shifts showed a striking critical point effect in all dopant/perturber systems. Our group also performed similar absorption measurements of atomic and molecular low-*n* Rydberg states in molecular perturbers [39, 40] with similar results. Because of the brevity of this Chapter, the details of these measurements cannot be presented here.

In all of the systems investigated [37–40], the dopant low-*n* Rydberg states are extremely sensitive to the nature of the perturbing fluid. When these states are doped into supercritical fluids, the surrounding perturbers interact with the central dopant causing shifts both in the dopant ground state energy and in the excited state energy. At low perturber number densities, the dopant/perturber interaction stabilizes the dopant ground state and the low-*n* Rydberg state. As the perturber density increases, perturber/dopant interactions lead to

the formation of a perturber solvent shell around the dopant core, thereby inducing local perturber density inhomogeneities. This solvent shell begins to shield the optical electron from the cationic core. Therefore, the dense perturber fluid increases the dopant excitation energy, resulting in a blue shift of the abosrption band, which is observed experimentally. The local density of the first perturber solvent shell is almost proportional to the perturber bulk density at non-critical temperatures. However, near the critical isotherm and critical density of the perturber, the dopant/perturber interactions strengthen due to the increased perturber/perturber correlation length. This increased order yields a corresponding increase of the local density in the solvent shell that, in turn, leads to a stronger shielding of the optical electron from the cationic core. Thus, increased blue shifts of the low-n absorption bands are observed in all dopant/perturber systems near the critical point of the perturber. The area of this critical effect is demarcated by the turning points that bound the saddle point in the thermodynamic phase diagram of the critical isotherm.

For fluids with similar compressibilities, the structures of low-n dopant Rydberg states in the perturbing fluid show systematic behaviors. At non-critical temperatures, $\Delta(\rho_P)$ is determined by the polarizability and size of the perturbing fluid. The larger the polarizability and, therefore, the larger the size, the smaller the perturber-induced energy shift of the dopant absorption bands. This is caused by the number of atoms that can exist between the optical electron and the dopant cationic core, coupled with the strength of the shielding. The large overall energy shift observed in the dopant low-n Rydberg states perturbed by CF_4 [39, 40], on the other hand, was caused by the larger compressibility of CF_4 in comparison to the other gases in this study [37, 38, 40]. This larger compressibility implies that CF_4 is closer together on average at high perturber number densities than are the other perturbers studied, which increases the local density of CF_4 and, therefore, increases the blue shift in this perturber.

The critical point effect, on the other hand, is dominated by the similarity of the perturber/perturber interaction with the dopant/perturber ground state and dopant/perturber excited state interactions, coupled with the overall local density of the system. In krypton, the well depth of the ground state perturber/perturber intermolecular potential and the dopant/perturber intermolecular potential shows greater similarity in comparison to that in Ar and Xe. Moreover, the excited state CH_3I/Kr interaction is slightly stronger than the ground state Kr/Kr interaction. These facts dictate that the largest critical point effect for CH_3I in atomic perturbers is in Kr. Similarly, the largest overall critical effect was observed in CH_3I/CH_4 [39, 40]. This large critical effect is caused by both the ground state and excited state CH_3I/CH_4 interactions having strengths comparable to the CH_4/CH_4 interaction. Although the excited state CH_3I/CF_4 interactions are comparable in strength to the CF_4/CF_4 interactions, the ground state CH_3I/CF_4 interactions are not close to those of CF_4/CF_4. Similarly, the Xe/CF_4 ground state interactions are comparable to the ground state CF_4/CF_4 interactions, but the excited state $Xe/$ground state CF_4 interactions are weaker. Moreover, the bulk critical density in CF_4 is small in comparison to the rest of the perturbers investigated here. This results in the CF_4 critical effect on $\Delta(\rho_P)$ being the smallest one observed [39, 40].

These data sets also allowed us to generate a consistent set of intermolecular potential parameters for various dopant/perturber systems, which are summarized in Appendix A. Several general trends in these parameters can be observed. For atomic perturbers, the steepness of the exponential-6 intermolecular potential (i.e., γ) used to model the

dopant excited state/perturber intermolecular interaction decreases with increasing perturber size and polarizability. This trend is reversed in molecular perturbers, were the larger, more compressible CF_4 has a steeper repulsive component in comparison to CH_4. The excited vibrational states of CH_3I always have exponential-6 potentials with a smaller γ in comparison to the CH_3I adiabatic transition in the same perturbing gas. Moreover, the vibrational states always have an equilibrium collision radius that is identical or larger than the collision radius of the adiabatic transition. The excited state collision radii are always larger than the ground state collision radii, as one would expect. However, the interaction strength of the excited state (as gauged by the well depth) can be stronger or weaker than that for the ground state of the same system. These changing interactions are what dominate the variations observed in the critical effects for each of the dopant/perturber systems investigated here.

An understanding of the structure of low-*n* Rydberg states in supercritical fluids is an important tool in the investigation of solvation effects, since these studies can yield accurate dopant/perturber ground state and excited state intermolecular potentials. We conclude from the present work that the absorption line shapes can be adequately simulated within a simple semi-classical line shape analysis. However, this work focused on highly symmetric perturbers. Future studies should concern more asymmetric perturbers and polar perturbers. Such an extension will require changing the calculation techniques involved in determining the radial distribution functions as well as the type of Fourier transform used to simulate the line shape. Since the excited state is sensitive to the structure of the perturbing fluid, we anticipate that multi-site intermolecular potentials and angular dependent intermolecular potentials will be needed as the perturber complexity increases, in order to model the full line shape accurately.

Acknowledgements

Author details

Luxi Li and Xianbo Shi
Brookhaven National Laboratory, Upton, NY, USA

Cherice M. Evans
Department of Chemistry, Queens College – CUNY and the Graduate Center – CUNY, New York, NY, USA

Gary L. Findley
Chemistry Department, University of Louisiana at Monroe, Monroe, LA, USA

Appendix A. Intermolecular potential parameters

Below is a tablulated list of the intermolecular potential parameters used to simulate the absorption line shapes in the various dopant/perturber systems presented or summarized in this work [40].

	ε/k_B (K)	r_e (Å)	γ	Ref.
Ar/Ar	119.5	3.826	–	[37, 38]
Kr/Kr	172.7	4.031	–	[38]
Xe/Xe	229.0	4.552	–	[38]
$CH_4/CH_4{}^a$	141.5	3.704	–	[39]
CF_4/CF_4	181.02	4.708	–	[39]
Xe/Ar	200.0	4.265	–	[37]
XeAr/Ar	195.0	4.310	–	[37]
Xe/CF_4	199.3	4.629	–	[39]
CH_3I/Ar	162.2	4.572	–	[38]
CH_3I/Kr	196.7	4.676	–	[38]
CH_3I/Xe	297.5	4.896	–	[38]
CH_3I/CH_4	195.8	4.243	–	[39]
CH_3I/CF_4	256.0	5.016	–	[39]
Xe $6s$/Ar	300.0	5.20	16.00	[37]
Xe $6s$/CF_4	135.0	6.55	12.25	[39]
$CH_3I\ 6s$/Ar	110.0	6.30	12.75	[38]
$CH_3I\ 6s$/Kr	245.0	6.20	11.30	[38]
$CH_3I\ 6s$/Xe	400.0	6.39	10.25	[38]
$CH_3I\ 6s$/CH_4	145.0	6.55	10.10	[39]
$CH_3I\ 6s$/CF_4	185.0	6.84	12.10	[39]
Xe $6s'$/Ar	400.0	4.98	16.00	[37]
$CH_3I\ 6s'$/Ar	110.0	6.30	12.75	[38]
$CH_3I\ 6s'$/Kr	245.0	6.20	11.30	[38]
$CH_3I\ 6s'$/Xe	400.0	6.29	10.25	[38]
$CH_3I\ 6s'$/CH_4	145.0	6.55	10.10	[39]
$CH_3I\ 6s'$/CF_4	185.0	6.84	12.10	[39]
Xe$(6s)$Ar/Ar	250.0	5.25	16.00	[37]
$CH_3I\ 6s\ \nu_2$/Ar	150.0	6.30	12.15	[38]
$CH_3I\ 6s\ \nu_2$/Kr	225.0	6.30	10.75	[38]
$CH_3I\ 6s\ \nu_2$/Xe	360.0	6.50	9.50	[38]
$CH_3I\ 6s\ \nu_2$/CH_4	105.0	6.65	9.95	[39]
$CH_3I\ 6s\ \nu_2$/CF_4	135.0	6.84	11.90	[39]
$CH_3I\ 6s'\ \nu_2$/Ar	150.0	6.30	12.15	[38]
$CH_3I\ 6s'\ \nu_2$/Kr	225.0	6.30	10.75	[38]
$CH_3I\ 6s'\ \nu_2$/Xe	360.0	6.35	9.50	[38]
$CH_3I\ 6s'\ \nu_2$/CH_4	105.0	6.65	9.95	[39]
$CH_3I\ 6s'\ \nu_2$/CF_4	135.0	6.84	11.90	[39]

[a] Two-Yukawa potential with $\kappa_0 = 8.50$ Å, $z_1 = 0.90$ Å^{-1}, and $z_2 = 4.25$ Å^{-1}.

6. References

[1] M. B. Robin. *Higher Excited States of Polyatomic Molecules Vol. I – Vol. III*. Academic Press, New York, 1974, 1975, 1985. and references therein.

[2] R. Reininger, U. Asaf, I. T. Steinberger, and S. Basak. Relationship between the energy v_0 of the quasi-free-electron and its mobility in fluid argon, krypton, and xenon. *Physical Review B*, 28(8):4426–4432, 1983.

[3] R. Reininger, U. Asaf, and I. T. Steinberger. The density dependence of the quasi-free electron state in fluid xenon and krypton. *Chemical Physics Letters*, 90(4):287–290, 1982.

[4] A. O. Allen and W. F. Schmidt. Determination of the energy level v_0 of electrons in liquid argon over a range of densities. *Zeitschrift für Naturforschung A*, 37(4):316–318, 1982.

[5] W. von Zdrojewski, J. G. Rabe, and W. F. Schmidt. Photoelectric determination of v_0-values in solid rare gases. *Zeitschrift fur Naturforschung A*, 35(7):672–674, 1980.

[6] B. Halpern, J. Lekner, S. A. Rice, and R. Gomer. Drift velocity and energy of electrons in liquid argon. *Physical Review*, 156(2):351–352, 1967.

[7] W. Tauchert, H. Jungblut, and W. F. Schmidt. Photoelectric determination of v_0 values and electron ranges in some cryogenic liquids. *Canadian Journal of Chemistry*, 55(11):1860–1866, 1977.

[8] J. R. Broomall, W. D. Johnson, and D. G. Onn. Density dependence of the electron surface barrier for fluid helium-3 and helium-4. *Physical Review B*, 14(7):2819–2825, 1976.

[9] J. Jortner and A. Gaathon. Effects of phase density on ionization processes and electron localization in fluids. *Canadian Journal of Chemistry*, 55(11):1801–1819, 1977.

[10] N. Schwenter, E. E. Koch, and J. Jortner. *Electronic Excitations in Condensed Rare Gases*. Springer-Verlag, Berlin, 1985.

[11] U. Asaf, R. Reininger, and I. T. Steinberger. The energy v_0 of the quasi-free electron in gaseous, liquid, and solid methane. *Chemical Physics Letters*, 100:363–366, 1983.

[12] C. M. Evans and G. L. Findley. Energy of the quasifree electron in argon and krypton. *Physical Review A*, 72:022717, 2005.

[13] C. M. Evans and G. L. Findley. Energy of the quasi-free electron in supercritical argon near the critical point. *Chemical Physics Letters*, 410:242–246, 2005.

[14] C. M. Evans and G. L. Findley. Field ionization of c$_2$h$_5$i in supercritical argon near the critical point. *Journal of Physics B: Atomic, Molecular and Optical Physics*, 38:L269–L275, 2005.

[15] Luxi Li, C. M. Evans, and G. L. Findley. Energy of the quasi-free electron in supercritical krypton near the critical point. *Journal of Physical Chemistry A*, 109:10683–10688, 2005.

[16] Xianbo Shi, Luxi Li, C. M. Evans, and G. L. Findley. Energy of the quasi-free electron in xenon. *Chemical Physics Letters*, 432:62–67, 2006.

[17] Xianbo Shi, Luxi Li, C. M. Evans, and G. L. Findley. Energy of the quasi-free electron in argon, krypton and xenon. *Nuclear Instruments and Methods in Physics Research A*, 582:270–273, 2007.

[18] Xianbo Shi, Luxi Li, G. M. Moriarty, C. M. Evans, and G. L. Findley. Energy of the quasi-free electron in low density ar and kr: extension of the local wigner-seitz model. *Chemical Physics Letters*, 454:12–16, 2008.

[19] Xianbo Shi, Luxi Li, G. L. Findley, and C. M. Evans. Energy of the excess electron in methane and ethane near the critical point. *Chemical Physics Letters*, 481:183–189, 2009.

[20] G. D. Mahan. Satellite bands in alkali-atom spectra. *Physical Review A*, 6:1273–1279, 1972.

[21] M. Lax. The franck-condon principle and its application to crystals. *Journal of Chemical Physics*, 20:1752–1760, 1952.

[22] R. Granier, M. C. Castex, J. Granier, and J. Romand. Perturbation of the xenon 1469 a. resonance line by various rare gases and hydrogen. *Comptes Rendus de l'Académie des Sciences B*, 264:778, 1967.

[23] M. C. Castex, R. Granier, and J. Romand. Perturbation of the 1236-a. resonance line of krypton and the 1295-a. resonance line of xenon by various rare gases. *Comptes Rendus de l'Académie des Sciences B*, 268:552, 1969.

[24] M. C. Castex. Absorption spectra of xenon-rare gas mixtures in the far uv region (1150-1500 å): high resolution analysis and first quantitative absorption measurements. *Journal of Chemical Physics*, 66:3854–3865, 1977.

[25] I. Messing, B. Raz, and J. Jortner. Medium perturbations of atomic extravalence excitations. *Journal of Chemical Physics*, 66:2239–2251, 1977.

[26] I. Messing, B. Raz, and J. Jortner. Solvent perturbations of extravalence excitations of atomic xenon by rare gases at high pressures. *Journal of Chemical Physics*, 66:4577–4586, 1977.

[27] I. Messing, B. Raz, and J. Jortner. Perturbations of molecular extravalence excitations by rare-gas fluids. *Chemical Physics*, 25:55–74, 1977.

[28] I. Messing, B. Raz, and J. Jortner. Medium effects on the vibrational structure of some molecular rydberg excitations. *Chemical Physics*, 23:351–355, 1977.

[29] A. M. Halpern. Iterative fourier reconvolution spectroscopy: van der waals broadening of rydberg transitions; the $\sim$b $\leftarrow$ $\sim$x (5p, 6s) transition of methyl iodide. *Journal of Physical Chemistry*, 96:2448–2455, 1992.

[30] T. Kalbfleisch, R. Fan, J. Roebber, P. Moore, E. Jacobson, and L.D. Ziegler. A molecular dynamics study of electronic absorption line broadening in high-pressure nonpolar gases. *Journal of Chemical Physics*, 103:7673–7684, 1995.

[31] R. Fan, T. Kalbfleisch, and L. D. Ziegler. A molecular dynamics analysis of resonance emission: optical dephasing and inhomogeneous broadening of ch_3i in ch_4 and ar. *Journal of Chemical Physics*, 104:3886–3897, 1996.

[32] T. S. Kalbfleisch, L. D. Ziegler, and T. Keyes. An instantaneous normal mode analysis of solvation: methyl iodide in high pressure gases. *Journal of Chemical Physics*, 105:7034–7046, 1996.

[33] S. A. Egorov, M. D. Stephens, and J. L. Skinner. Absorption line shapes and solvation dynamics of ch_3i in supercritical ar. *Journal of Chemical Physics*, 107:10485–10491, 1997.

[34] E. Morikawa, A. M. Köhler, R. Reininger, V. Saile, and P. Laporte. Medium effects on valence and low-*n* rydberg states: No in argon and krypton. *Journal of Chemical Physics*, 89:2729–2737, 1988.

[35] P. Larrégaray, A. Cavina, and M. Chergui. Ultrafast solvent response upon a change of the solute size in non-polar supercritical fluids. *Chemical Physics*, 308:13–25, 2005.

[36] C. N. Tiftickjian and S. A. Egorov. Absorption and emission lineshapes and solvation dynamics of no in supercritical ar. *Journal of Chemical Physics*, 128:114501, 2008.

[37] Luxi Li, Xianbo Shi, C. M. Evans, and G. L. Findley. Xenon low-*n* rydberg states in supercritical argon near the critical point. *Chemical Physics Letters*, 461:207–210, 2008.

[38] Luxi Li, Xianbo Shi, C. M. Evans, and G. L. Findley. Ch_3i low-*n* rydberg states in supercritical atomic fluids near the critical point. *Chemical Physics*, 360:7–12, 2009.

[39] Luxi Li, Xianbo Shi, G. L. Findley, and C. M. Evans. Dopant low-*n* rydberg states in cf$_4$ and ch$_4$ near the critical point. *Chemical Physics Letters*, 482:50–55, 2009.

[40] Luxi Li. *Atomic and Molecular Low-n Rydberg States in Near Critical Point Fluids*. PhD thesis, The Graduate Center of the City University of New York, New York, NY, 2009.

[41] S. C. Tucker. Solvent density inhomogeneities in supercritical fluids. *Chemical Reviews*, 99:391–418, 1999.

[42] P. Attard. Spherically inhomogeneous fluids. i. percus-yevick hard spheres: osmotic coefficients and triplet correlations. *Journal of Chemical Physics*, 91:3072–3082, 1989.

[43] P. Attard. Spherically inhomogeneous fluids. ii. hard-sphere solute in a hard-sphere solvent. *Journal of Chemical Physics*, 91:3083–3089, 1989.

[44] J. Zhang, D. P. Roek, J. E. Chateauneuf, and J. F. Brennecke. A steady-state and time-resolved fluorescence study of quenching reactions of anthracene and 1,2-benzanthracene by carbon tetrabromide and bromoethane in supercritical carbon dioxide. *Journal of the American Chemical Society*, 119:9980–9991, 1997.

[45] Y. P. Sun, M. A. Fox, and K. P. Johnston. Spectroscopic studies of p-(n,n-dimethylamino)benzonitrile and ethyl p-(n,n-dimethylamino)benzoate in supercritical trifluoromethane, carbon dioxide, and ethane. *Journal of the American Chemical Society*, 114:1187–1194, 1992.

[46] R. S. Urdahl, D. J. Myers, K. D. Rector, P. H. Davis, B. J. Cherayil, and M. D. Fayer. Vibrational lifetimes and vibrational line positions in polyatomic supercritical fluids near the critical point. *Journal of Chemical Physics*, 107:3747–3757, 1997.

[47] R. S. Urdahl, K. D. Rector, D. J. Myers, P. H. Davis, and M. D. Fayer. Vibrational relaxation of a polyatomic solute in a polyatomic supercritical fluid near the critical point. *Journal of Chemical Physics*, 105:8973–8976, 1996.

[48] R. P. Futrelle. Unified theory of spectral line broadening in gases. *Physical Review A*, 5:2162–2182, 1972.

[49] J. L. Lebowitz and J. K. Percus. Statistical thermodynamics of nonuniform fluids. *Journal of Mathematical Physics*, 4:116–123, 1963.

[50] J. L. Lebowitz and J. K. Percus. Asymptotic behavior of radial distribution function. *Journal of Mathematical Physics*, 4:248–254, 1963.

[51] J. L. Lebowitz and J. K. Percus. Integral equations and inequalitites in theory of fluids. *Journal of Mathematical Physics*, 4:1495–1506, 1963.

[52] M. Born and H. S. Green. A general kinetic theory of liquids. i. the molecular distribution functions. *Proceedings of the Royal Society of London Series A*, 188:10–18, 1946.

[53] R. Kubo and Y. Toyozawa. Application of the method of generating function to radiative and non-radiative transitions of a trapped electron in a crystal. *Progress of Theoretical Physics*, 13:160–182, 1955.

[54] H. C. Jacobson. Moment analysis of atomic spectral lines. *Physical Review A*, 4:1363–1368, 1971.

[55] T. R. Strobridge. The thermodynamic properties of nitrogen from 64 to 300 °k between 0.1 and 200 atmospheres. *NBS Technical Note*, 129, 1962.

[56] A. L. Gosman, R. D. McCarty, and J. G. Hust. Thermodynamics properties of argon from the triple point to 300 k at pressures to 1000 atmsptheres. *NBS Technical Note*, 27, 1969.

[57] W. B. Streett and L. A. K. Staveley. Experimental study of the equation of state of liquid krypton. *Journal of Chemical Physics*, 55:2495–2506, 1971.

[58] W. B. Streett, L. S. Sagan, and L. A. K. Staveley. Experimental study of the equation of state of liquid xenon. *Journal of Chemical Thermodynamics*, 5:633–650, 1973.

[59] E. W. Grundke, D. Henderson, and R. D. Murphy. Evaluation of the percus-yevick theory for mixtures of simple liquids. *Canadian Journal of Physics*, 51:1216–1226, 1973.

[60] W. H. Press, S. A. Teukolsky, W. T. Vetterling, and B. P. Flannery. *Numerical Recipes in FORTRAN: The Art of Scientific Computing*. Cambridge University Press, New York, 1992.

[61] Xianbo Shi. *Energy of the Quasi-free Electron in Atomic and Molecular Fluids*. PhD thesis, The Graduate Center of the City University of New York, New York, NY, 2010.